https://doi.org/10.5194/wes-2025-264
Preprint. Discussion started: 4 December 2025

eawe european academy of wind energy
Open Access WIND ENERGY SCIENCE DISCUSSIONS

Dynamics of floating wind turbine wakes in a wind tunnel setup

Ricardo Amaral[1], Felix Houtin-Mongrolle[2], Dominic von Terzi[1], Kasper Laugesen[3], Paul Deglaire[4], and Axelle Viré[1]

[1]Delft University of Technology, Wind Energy Section, Kluyverweg 1, 2629 HS Delft, Netherlands
[2]Siemens Gamesa Renewable Energy (SGRE), Prinses Beatrixlaan 800, 2595 BN Den Haag, Netherlands
[3]Siemens Gamesa Renewable Energy (SGRE), Borupvej 16, 7330 Brande, Denmark
[4]Siemens Gamesa Renewable Energy (SGRE), Avenue de l'Université C/O Insa Rouen - BP 08, 76800 Saint Étienne de Rouvray, France

Correspondence: Ricardo Amaral (r.pintoelisbaomartinsamaral@tudelft.nl)

Abstract. The wake of a laboratory-scale wind turbine model is investigated in high-detail in a wind tunnel setup under prescribed surge, sway, roll, pitch, yaw and coupled surge-pitch motions using large-eddy simulations coupled to an actuator-line model. The goal is to assess how the wake of a moving turbine evolves in a high blockage ratio scenario and how it compares with the results found in the literature for full-scale models and experiments. This manuscript also extends the state-of-the-art to more degrees-of-freedom. Two cases per degree-of-freedom are considered: one with a low Strouhal number St and high normalized amplitude A^*, and vice versa. Cases with low-St/high-A^* exhibit a wake behavior similar to the fixed-bottom case. Conversely, cases with a high-St/low-A^* disturb the wake to a much larger extent. The contrast is caused by differences in how much the wake amplifies the perturbations of the floating motion upstream and is particularly noticeable at the blade tip and root trails. Prescribed motions with a component perpendicular to the flow are found to have a larger impact than motions exclusively in the flow direction. Overall, the phenomena found in the literature are well captured in this setup.

1 Introduction

In September 2024, Europe had 35 GW of installed offshore wind power capacity. The capacity is set to grow to 54 GW by 2030 (Costanzo et al., 2024). Most offshore wind turbines installed are fixed-bottom wind turbines, since they are more cost-competitive than floating offshore wind turbines (FOWTs) for water depths below 50-60 m (Cozzi et al., 2019; Barooni et al., 2023). However, harvesting wind energy in locations with water depths higher than 60 m, and more than 60 km away from the shore, has the potential to supply the world's total electricity demand several times by 2040 (Cozzi et al., 2019). At these depths, FOWTs are more cost-competitive, making the technology a serious candidate to support the energy transition. As a result, FOWT farms are already under operation, deployment and auction, with 10 GW of capacity expected in Europe by 2030 (WindEurope, 2022).

One way of maximizing the energy yield in wind farms is by improving the wake recovery of each individual turbine. The fact that the rotor is free to move in FOWTs when subjected to wind and sea states provides an unique opportunity to do that passively through structural design, which requires modeling the effect of the rotor motion on wakes. However, most engineering wake models do not intrinsically solve the time-varying nature of the wake (Jensen, 1983; Katic et al.,

https://doi.org/10.5194/wes-2025-264
Preprint. Discussion started: 4 December 2025

eawe european academy of wind energy
Open Access WIND ENERGY SCIENCE DISCUSSIONS

1986; Ainslie, 1988; Larsen, 2009; Bastankhah and Porté-Agel, 2014) and cannot capture this effect. Even the dynamic wake meandering model (Larsen et al., 2007) that captures this time dependence assumes that a base stationary wake is convected as a passive scalar subjected to large-scale ambient turbulent structures, thus neglecting the flow perturbation caused by the FOWT. As a consequence, a substantial amount of research has been conducted in recent years with the aim of understanding the factors driving wake dynamics.

It is now widely accepted that the wake acts as an amplifier of upstream perturbations and that these amplified perturbations drive wake meandering and tip and root vortex breakdown (Mao and Sørensen, 2018; Gupta and Wan, 2019; Li et al., 2022; Hodgson et al., 2023; Messmer et al., 2024). Moreover, this amplification is selective, depending on the frequency and amplitude of the perturbations as well as on the region of the wake and its characteristics (Mao and Sørensen, 2018; Gupta and Wan, 2019; Li et al., 2022; Hodgson et al., 2023; Messmer et al., 2024). The breakdown of the tip vortex sheet in particular, appears to be the key event that triggers a steeper wake recovery, as its presence insulates the inner wake from the free stream, preventing net momentum entrainment (Medici, 2005; Lignarolo et al., 2015; De Cillis et al., 2020). Several studies suggest that wakes tend to amplify frequencies in the vicinity of a peak Strouhal number St in the range of 0.1-0.9, (Medici and Alfredsson, 2006; Chamorro and Porté-Agel, 2010; Chamorro et al., 2013; Okulov et al., 2014; Howard et al., 2015; Heisel et al., 2018; Gupta and Wan, 2019; Hodgson et al., 2023; Messmer et al., 2024) and that perturbations in this range, induced by the inflow itself or by the movement of the turbine, lead to early tip vortex sheet breakdown, stronger meandering and enhanced recovery (Mao and Sørensen, 2018; Gupta and Wan, 2019; Li et al., 2022; Hodgson et al., 2023; Messmer et al., 2024). This results from shifting the streamwise position at which the recovery gradient increases sharply (Messmer et al., 2024), which coincides approximately with the point where the tip shear layers merge and the wake transitions to the far wake (Kang et al., 2014; Messmer et al., 2024). In the presence of both inflow perturbations (i.e. turbulence) and turbine movement, larger turbulence intensity (TI) values seem to accelerate the transition to the far wake and appear to contribute equally or even more to the transition than the turbine movement at relatively low values of TI (Li et al., 2022). This is nevertheless dependent on the turbulent time scales as smaller values of St in the range of $0.3 - 0.7$ (Hodgson et al., 2023) stimulate the transition while higher values slow it down (Hodgson et al., 2023; Gambuzza and Ganapathisubramani, 2023).

The prior work conducted by the scientific community provides a very consistent understanding of wake dynamics and its driving factors. The work presented herein aims at assessing how the wake of a moving turbine evolves in the POLIMI wind tunnel in the context of the UNAFLOW project and the OC6 task phase 3 (Fontanella et al., 2021a, b; Bergua et al., 2023; Cioni et al., 2023), which is a high blockage ratio setup, and how it compares with the results found in the literature for full-scale models and experiments. It also extends this analysis to inflow perturbations originating from floating turbine motions in a larger set of DOFs, while providing an holistic comparison among them. This is done by considering two different cases per DOF: one with a low Strouhal number St and high normalized amplitude A^*, and vice versa. The differences among DOFs and St-A^* pair are then analyzed in detail in terms of wake recovery, turbulence intensity, frequency contents, tip and root vortex trails and wake meandering.

https://doi.org/10.5194/wes-2025-264
Preprint. Discussion started: 4 December 2025

eawe european academy of wind energy
Open Access WIND ENERGY SCIENCE DISCUSSIONS

2 Methodology

2.1 Numerical framework

Studying wind turbine wakes in detail requires the use of high-fidelity techniques at high mesh resolutions to capture the small scales that may be determinant in driving the wake evolution. Large-eddy simulations provide a suitable method that consists in spatially filtering the Navier-Stokes (NS) equations with a filter size somewhere in the inertial range. For a constant density fluid, the filtered NS equations are:

$$\frac{\partial \widetilde{u}_j}{\partial t} + \frac{\partial \widetilde{u}_i \widetilde{u}_j}{\partial x_i} = -\frac{1}{\rho}\frac{\partial \widetilde{p}}{\partial x_j} - \frac{\partial \tau_{ij}^{\mathrm{r}}}{\partial x_i} + \nu \frac{\partial^2 \widetilde{u}_j}{\partial x_i \partial x_i} + \frac{\widetilde{f}_j}{\rho} \qquad \text{and} \qquad \frac{\partial \widetilde{u}_i}{\partial x_i} = 0, \tag{1}$$

where Einstein's notation is used, $\widetilde{\cdot}$ is the filtering operator, u is the velocity vector, p is the pressure, ν is the kinematic viscosity, ρ is the density and f the external volume forces. The subgrid scale stress tensor τ_{ij}^{r} was based on the dynamic Smagorinsky model (Germano et al., 1990). The turbine was modeled with an actuator-line model (ALM) (Sorensen and Shen, 2002). The equations were solved using the YALES2 flow solver (Moureau et al., 2011), which is a massively parallel finite-volume solver specifically tailored for LES. YALES2 relies on a central 4th-order numerical scheme for spatial discretization, and a method similar to the 4th-order Runge-Kutta method (Kraushaar, 2011) for the time integration. The discretization is strictly fourth-order on Cartesian grids. On tetrahedral grids with homogeneous cell size, the spatial errors are fourth-order but this order of convergence can decrease on low quality grids. YALES2's ALM implementation is described by Houtin-Mongrolle (2022). The necessity of fairly high-order numerics to ensure the proper transport of fine vortical structures, in the context of ALM, was demonstrated by Benard et al. (2018), where they advise a minimum grid resolution at the rotor and wake regions and actuator line discretization in unstructured meshes of $D/\Delta x \approx 66$ for proper results.

2.2 Wind turbine model and floating degrees-of-freedom

The simulation setup was the one from the UNAFLOW project and the OC6 task phase 3 (Fontanella et al., 2021a, b; Bergua et al., 2023; Cioni et al., 2023), and hence, reproduced the cross-section of the POLIMI wind tunnel and the wind turbine model used in the experiment. The model was a laboratory-scale DTU 10 MW wind turbine (Bak et al., 2013; Bayati et al., 2017; Fontanella et al., 2021b). The model was scaled-down using the length and velocity scaling factors $\lambda_L = D_{DTU10MW}/D_{Model} = 75$ and $\lambda_{U_R} = U_{R_{DTU10MW}}/U_{R_{Model}} = 3$, where D is the turbine diameter and U_R is the rated wind speed. Moreover, it was designed to have the same thrust coefficient curve as the DTU 10 MW, at lower rated wind speed, by means of low-Re number airfoils (Bayati et al., 2017), where Re is the Reynolds number. Some standard features of the model can be seen in Table 1. Fig. 1 (a) shows the model in perspective, where the rotor rotates clockwise. The turbine configuration was the same as the one used in the IEA task OC6 Phase III (Bergua et al., 2023; Cioni et al., 2023; Fontanella et al., 2021a, b) and this can be seen in Fig. 1 (b). No tower, nacelle nor hub were simulated but these components are shown in Fig. 1 (b) because their dimensions were taken into account when prescribing motions in rotational DOFs. The setup dimensions are shown in Table 2, where a difference in hub height between translation and rotation cases is present, as per the experimental

https://doi.org/10.5194/wes-2025-264
Preprint. Discussion started: 4 December 2025

eawe european academy of wind energy
Open Access WIND ENERGY SCIENCE DISCUSSIONS

setup. It is important to notice two things. First, the rotor tilt and the angle α cancel out so that the rotor is perpendicular to the free-stream velocity. This was done to isolate the prescribed motion effects from the rotor tilt effects. Second, the turbine was closer to the top wall than to the bottom wall. Only the hub height is given in Table 2 for the translation configuration since the prescribed motion velocity was the same for every point in the rotor.

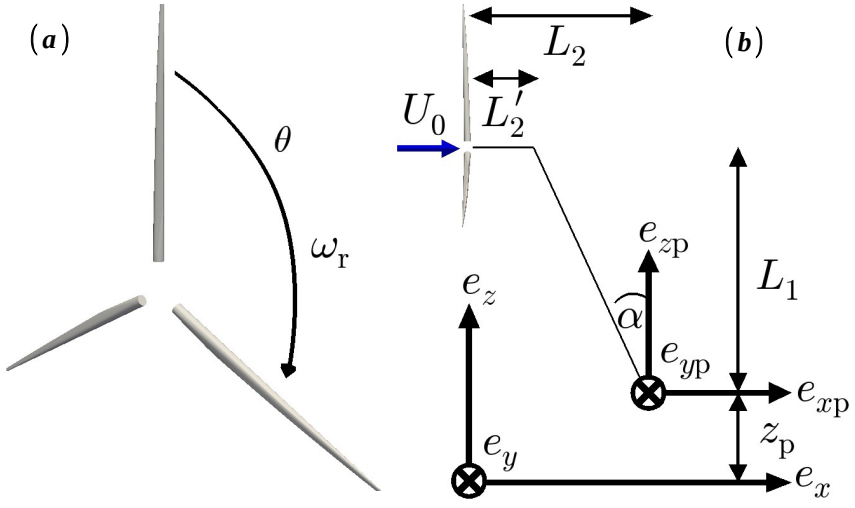

Figure 1. Simulated components (blades) in perspective (a) and initial turbine setup with reference frames (b).

Table 1. Turbine characteristics and operating conditions.

Rotor diameter	Hub diameter	Blade length	Rotor tilt	Rated wind speed	Rotor speed	Tip-speed ratio
D	D_h	L_b	-	U_R	ω_r	λ
2.381 m	0.178 m	1.102 m	5 deg	4 ms^{-1}	240 rpm	7.476

Table 2. Turbine setup dimensions.

	z_p	L_1	$L_{2'}$	L_2	α	$z_\mathrm{rc} = z_\mathrm{p} + L_1$
Translation	-	-	-	-	5 deg	2.086 m
Rotation	0.730 m	1.458 m	0.139 m	0.267 m	5 deg	2.188 m

Two reference frames can be identified in Fig. 1 (b). The global reference frame is the frame $\boldsymbol{e_x}$-$\boldsymbol{e_y}$-$\boldsymbol{e_z}$ which is centered at point $(0,0,0)$ and is fixed. $\boldsymbol{e_y}$ follows the right-hand rule. The initial coordinates of the rotor center in this frame are $(0,0,z_\mathrm{rc})$. The surge, sway and heave motions are, respectively, translations in the $\boldsymbol{e_x}$, $\boldsymbol{e_y}$ and $\boldsymbol{e_z}$ directions and are defined relative to the global reference frame. The prescribed reference frame is the frame $\boldsymbol{e_{xp}}$-$\boldsymbol{e_{yp}}$-$\boldsymbol{e_{zp}}$ which is centered at the tower bottom and

https://doi.org/10.5194/wes-2025-264
Preprint. Discussion started: 4 December 2025

translates with the turbine. $\boldsymbol{e_{yp}}$ follows the right-hand rule. The roll, pitch and yaw motions are, respectively, the rotations about the $\boldsymbol{e_{xp}}$, $\boldsymbol{e_{yp}}$ and $\boldsymbol{e_{zp}}$. All the aforementioned motions are defined in the floating foundation context and can be visualized in Fig. 2. The prescribed motions were of the form:

$$p = \pm A_{\mathrm{p}} \sin(\omega_{\mathrm{p}} t), \tag{2}$$

where p is the corresponding prescribed motion (in length units for translation and angle units for rotations), A_{p} is the prescribed motion amplitude and $\omega_{\mathrm{p}} = 2\pi f_{\mathrm{p}}$ is the prescribed motion angular frequency. The prescribed motion capability was implemented in YALES2 in order to perform the simulations (see the validation in Appendix A).

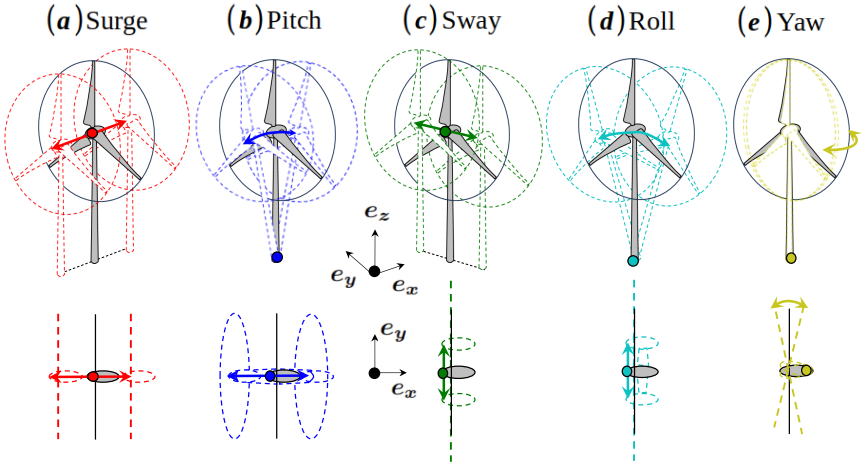

Figure 2. Floating foundation DOFs and the motion they induce on the turbine.

2.3 Case description

The turbine was modeled as rigid and operated near rated conditions, under constant rotor angular velocity $\omega_{\mathrm{r}} = 240$ rpm and steady uniform free-stream velocity of magnitude $U_0 = U_R = 4$ ms^{-1}. This reproduces the conditions in the UNAFLOW project and the OC6 task phase 3 (Fontanella et al., 2021a, b; Bergua et al., 2023; Cioni et al., 2023), except for the turbulence intensity of the inflow which was around 2% in the experiment. This simplification was done since the turbulence intensity value was relatively low and in order to focus the analysis on the unsteady wake effects induced by the turbine motion, similarly to what was done by Messmer et al. (2024). The operating conditions are summarized in Table 1. The simulated cases are described in Table 3. The f_{p}-A_{p} pairs for single-DOF surge and pitch were taken directly from the UNAFLOW project and the OC6 task phase 3 (Fontanella et al., 2021a, b; Bergua et al., 2023; Cioni et al., 2023) case definition. The table shows the amplitudes prescribed in each DOF A_{p}, the corresponding non-dimensional values of the prescribed motion amplitude at the rotor center A^*_{prc}, the prescribed motion frequency f_{p}, and its non-dimensional value or Strouhal number St_{p}. The subscripts "p", "r" and "c" stand for "prescribed", "rotor" and "center". The superscript * indicates that a quantity was normalized by the

https://doi.org/10.5194/wes-2025-264
Preprint. Discussion started: 4 December 2025

eawe european academy of wind energy
Open Access WIND ENERGY SCIENCE DISCUSSIONS

simulated laboratory-scale turbine diameter D. The prescribed Strouhal number was defined by:

$$St_{\mathrm{p}} = \frac{f_{\mathrm{p}} D}{U_0}, \tag{3}$$

Table 3. Case definition.

Case	DOF	$f_{\mathrm{p}}\ [Hz]$	$St_{\mathrm{p}}\ [-]$	A_{p}	$A^*_{\mathrm{prc}}\ [-]$
FB	Fixed-bottom	0 m	0	0	0
SuLS	Surge	0.125	0.0744	0.125 m	0.0525
SuHS	Surge	2.000	1.1905	0.008 m	0.0034
PiLS	Pitch	0.125	0.0744	3.0 deg	0.0326
PiHS	Pitch	2.000	1.1905	0.3 deg	0.0033
SuPiLS	Surge, Pitch	0.125	0.0744	0.125 m, 3.0 deg	0.0851
SuPiHS	Surge, Pitch	2.000	1.1905	0.008 m, 0.3 deg	0.0067
SwLS	Sway	0.125	0.0744	0.125 m	0.0525
SwHS	Sway	2.000	1.1905	0.008 m	0.0034
RoLS	Roll	0.125	0.0744	3.0 deg	0.0321
RoHS	Roll	2.000	1.1905	0.3 deg	0.0032
YaLS	Yaw	0.125	0.0744	3.0 deg	0.0268
YaHS	Yaw	2.000	1.1905	0.3 deg	0.0027

The cases were named with the two first letters of the DOF of the prescribed motion (e.g "Su" for surge). These letters are followed by either "LS" or "HS" standing for "Low Strouhal" or "High Strouhal", respectively. The dimensional values f_{p} and A_{p} were scaled down from the corresponding values of the DTU 10 MW using the length and velocity scaling factors of the model, described in Section 2.2. For the translational DOFs, $A^*_{\mathrm{prc}} = A_{\mathrm{p}}/D$. For rotational DOFs, $A^*_{\mathrm{prc}} = A_{\mathrm{p}} L_{\mathrm{rot}}/D$, where L_{rot} is the distance perpendicular to the rotation point. For the coupled surge-pitch cases, the amplitudes were obtained by summing the amplitudes of the corresponding single-DOF surge and pitch cases, since the pitch amplitudes were small. All the amplitudes were defined relative to the initial turbine setup in Fig. 1 (b). The same St set was used for all DOFs. Surge and sway were simulated with the same amplitude set. Similarly, roll, pitch and yaw were also simulated with the same amplitude set. While the f_{p}-A_{p} pairs for single-DOF surge and pitch were realistic, the amplitudes for the remaining cases were over what one would normally expect for a FOWT, since the largest amplitudes tend to occur in the flow direction. Nevertheless, this allowed for a comparison at similar magnitudes of prescribed motion among translation DOFs and among rotation DOFs, opening the possibility to explore what phenomena could be triggered if one purportedly designed for larger sway, roll and yaw as a way to boost wake recovery. The validation of the prescribed motion implementation is provided in Appendix A.

https://doi.org/10.5194/wes-2025-264
Preprint. Discussion started: 4 December 2025

eawe european academy of wind energy
Open Access WIND ENERGY SCIENCE DISCUSSIONS

2.4 Computational setup

The rotor was placed in a computational domain of dimensions $19D \times 5.8D \times 1.6D$ and centered at a distance $5D$ from the domain inlet. The domain reproduced the POLIMI wind tunnel cross-section while the length of the domain was made larger so as to place the turbine farther away from the inlet and the outlet. This resulted in a blockage ratio of 8.46%. In the wind tunnel, the flow was naturally sheared near the walls but these were modeled as slip walls in the simulations. This choice was made to prioritize a high level of refinement in the wake region, while keeping the computational cost in check. The mesh was unstructured and composed of around 318 million tetrahedral elements. Figure 3 (a) and (b) show a longitudinal and transversal slice depicting the domain dimensions and refinement regions with the corresponding normalized mesh resolution $D/\Delta x$, where Δx is the cell size. $D/\Delta x$ is the inverse of the normalized cell size and represents how many actuator points would exist in a rotor diameter, given the cell size of the point in question. Two refinement levels were used. The wake refinement level is the high-refinement region with a average and maximum cell size in the vicinity of the rotor equal to 2.5×10^{-2} m and 3.2×10^{-2} m, respectively. This region was cylindrical with a radius and length of approximately $1D$ and $8.5D$. The number of actuator points in the rotor was set according to the maximum cell size and yielded 66 actuator points per diameter. The smearing parameter was set to $\epsilon/\Delta x = 2$ (Troldborg et al., 2009). The cell size grew at a rate of 1.07 from the wake refinement to the background refinement at the domain boundaries. The background refinement had a minimum resolution of nine actuator-points per diameter.

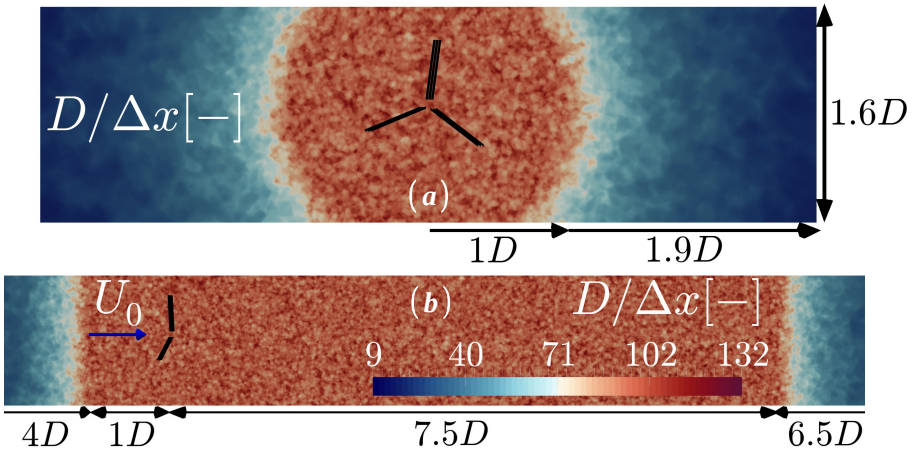

Figure 3. Longitudinal slice of the domain (a) and transversal slice of the domain (b) showing the normalized mesh resolution. The inlet and outlet were trimmed in (b).

The simulations were carried out with a variable time step that was set such that $CFL \leq 0.9$ for every cell and time instant, where $CFL = ||u||\Delta t/\Delta x$ is the Courant–Friedrichs–Lewy number. The simulations were performed during 64 s and the statistics were taken in the last 32 s (see Appendix B for the time convergence validation). The airfoils' Re were found to be within 5% of their actual Re for the fixed-bottom case in the most loaded blade region, between $s \approx 30\ \%$ and $s \approx 97\ \%$, where

https://doi.org/10.5194/wes-2025-264
Preprint. Discussion started: 4 December 2025

eawe european academy of wind energy
Open Access WIND ENERGY SCIENCE DISCUSSIONS

s is the spanwise position. Finally, a comparison with experimental loads results is included in the Appendix C. The match between the simulations and the experiments was not perfect but there were difficulties on both sides that may have contributed to the mismatch. All in all, the simulation setup was considered to be acceptable for the studies presented in this manuscript. This decision was supported by the fact that the wake behavior is mostly driven by the operating point of the turbine, the thrust coefficient and the floating turbine motion. Similarly to the experimental cases, the turbine operated near rated conditions in the C_p-maximizing region. The mean thrust coefficient was, at most, 8% above or below the experimental values. The thrust amplitude of cases SuLS and PiLS was, at most, 10% below or above the experimental values. The thrust amplitude of cases SuHS and PiHS showed larger differences but may be explained by the higher uncertainty in the measurements associated with the inertial loads Bergua et al. (2023) and the prescribed amplitude mismatch between the experimental data of PiHS (0.26 deg) and the load case definition (0.3 deg).

2.5 Data extraction

The wake was characterized by extracting the time series of the three flow field velocity components at several streamwise positions, by means of radial probes, as the ones shown in Fig. 4. Each radial probe was composed of 98 linear sub-probes dispersed azimuthally with a uniform angular spacing and discretized in 41 points in the radial direction. The number of sub-probes and their points was a compromise between spatial resolution and data size. The radial probe radius was $1.25D$ with a radial resolution of about $33/D$ and a minimum azimuthal resolution at the rotor perimeter of about $31/D$. The time series were acquired at each point in the probe. The probes' axes were aligned with the initial rotor axis throughout the simulation and did not move with the turbine.

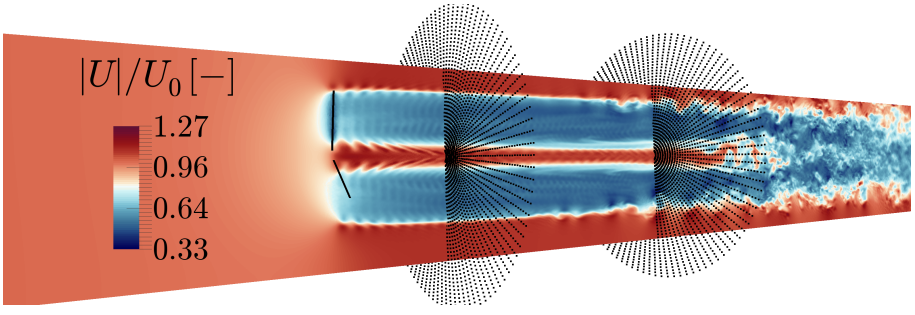

Figure 4. Two radial probes superimposed on a vertical domain slice. The slice was colored by the streamwise velocity contours at $t/T_\mathrm{p} = 4$ for the SuLS case, where $T_\mathrm{p} = 1/f_\mathrm{p}$.

https://doi.org/10.5194/wes-2025-264
Preprint. Discussion started: 4 December 2025

eawe european academy of wind energy
Open Access WIND ENERGY SCIENCE DISCUSSIONS

3 Results

3.1 Wake recovery

The first question that was investigated was the effect of the prescribed motion on the mean wake and the consequences on the wake recovery. As a result, the normalized time-averaged streamwise flow velocity $<U_x>/U_0$ was looked at in the radial probes, where $<\cdot>$ denotes the time average. The streamwise evolution of $<U_x>/U_0$ can be seen in Fig. 5 for several cases. The black dashed circle indicates the rotor perimeter. The black region on the top of each contour corresponds to the upper wall. Each row represents one downstream position while each column represents one case. The smooth plots were obtained via linear interpolation. Looking at the FB case, the time-averaged wake expanded steadily downstream while conserving the circular shape. This was a pattern that was observed for the SuLS, SuHS and SwLS cases but not for the SwHS case which developed more irregular and smeared-out edges. Although not shown, all of the low-St/high-A^* cases behaved similarly to the former cases while all of the high-St/low-A^* cases (except the SuHS case) behaved similarly to the latter case. These results suggest that exciting the wake at the high-St/low-A^* leads to more destabilization at its outer boundary than with the low-St/high-A^*. They also suggest that exciting the wake at least in one direction perpendicular to the flow, i.e. all DOFs but surge, leads to more destabilization than exciting the wake exclusively in the flow direction, i.e. surge.

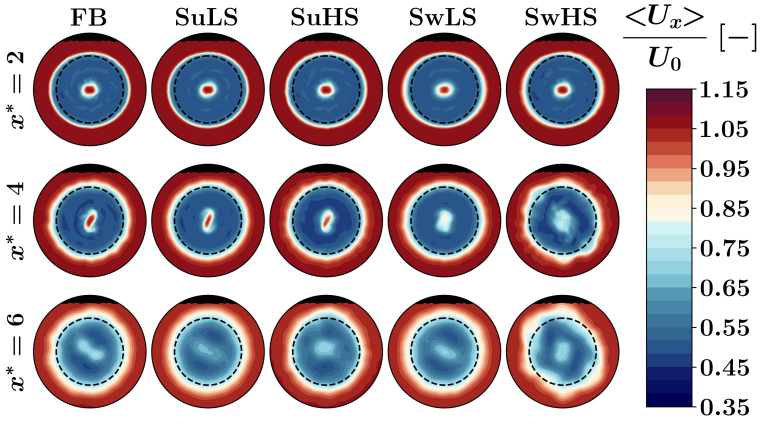

Figure 5. Normalized time-averaged streamwise velocity over the radial probes at several streamwise positions. The black region corresponds to the upper wall.

In order to compare the cases in a practical way, the spatially averaged values of $<U_x>/U_0$ were computed over the area between the hub and the rotor radius for each radial probe. This quantity was simply called "wake recovery" throughout the paper. The hub area was excluded to limit the impact of the absence of the nacelle. For a general variable X, the spatial

https://doi.org/10.5194/wes-2025-264
Preprint. Discussion started: 4 December 2025

eawe european academy of wind energy
Open Access WIND ENERGY SCIENCE DISCUSSIONS

averaging was computed as:

$$\overline{X} = \frac{\int_0^{2\pi}\int_{r_\mathrm{h}}^{r_\mathrm{r}} X\ r dr d\theta}{\int_0^{2\pi}\int_{r_\mathrm{h}}^{r_\mathrm{r}} r dr d\theta}, \tag{4}$$

where $\overline{\ }$ denotes the spatial average, r_r is the rotor radius and r_h is the hub radius. The wake recovery excess due to the prescribed motion was defined as the difference in wake recovery relative to the FB case:

$$\Delta_\mathrm{FB} = \frac{\overline{<U_x>}}{U_0} - \left.\frac{\overline{<U_x>}}{U_0}\right|_\mathrm{FB}, \tag{5}$$

and was used to quantify the effect of the prescribed motion on the wake recovery. Positive values of this quantity indicate that the wake recovery value is higher than that of the FB case for a given downstream position, and vice-versa. Similarly, the wake recovery gradient excess due to the prescribed motion was estimated through the slope of the previous equation normalized by $1/D$:

$$D\frac{\partial \Delta_\mathrm{FB}}{\partial x} = \frac{D}{U_0}\left(\frac{\partial\overline{<U_x>}}{\partial x} - \left.\frac{\partial\overline{<U_x>}}{\partial x}\right|_\mathrm{FB}\right), \tag{6}$$

where the slope was calculated using forward finite differences. This represented the difference in how fast the wake recovered as it moved downstream, when compared to the FB case. Positive values of this quantity indicate that the wake was recovering faster than the FB case for a given downstream position, and vice-versa. Figure 6 shows (a) $\overline{<U_x>}/U_0$, (b) Δ_FB and (c) $D\partial\Delta_\mathrm{FB}/\partial x$ for several streamwise positions. Δ_{FB} and $D\partial\Delta_{FB}/\partial x$ are both absolute differences between physical quantities measured in percentage, hence they are also measured in percentage. Figure 6 (a) illustrates the wake recovery profile for the FB case which is representative of the shape of the remaining cases' profiles. Although not shown, all cases show the minimum $\overline{<U_x>}/U_0$, i.e. the onset of the wake recovery, at $x^* = 3$, with the exception of cases SwHS and RoHS, whose minimum is located at $x^* = 2$. Looking at Fig. 6 (b), the high-St/low-A^* cases exhibited higher wake recovery than the low-St/high-A^* cases, with the exception of the SuHS case that seemed to hamper the recovery between $x^* = 4$ and $x^* = 7$. The low-St/high-A^* cases also led to higher wake recovery when compared to the FB case, but the improvement was smaller. The wake recovery gradients of Fig. 6 (c) were generally above the FB case upstream and downstream but not in the middle. An interesting point of the analysis is the effect of coupling surge and pitch. The addition of the surge motion to the pitch motion (cases SuPiLS and SuPiHS) appeared to originate wake recovery excess and wake recovery gradient excess profiles that were the sum of the individual profiles to some degree. For instance, the SuPiHS case had a lower recovery and recovery gradient than PiHS, as per the negative effect of SuHS. The final value of the recovery was very close to that of pitch, as the wake recovery excess of SuHS went from negative to zero. Similar effects were also observed on the recovery gradient and the SuLS, PiLS and SuPiLS cases.

Another evidence of the difference between disturbing the flow perpendicularly to it versus in its direction can be found by comparing the SwHS and RoHS cases to the SuHS and SuPiHS cases and the PiHS and YaHS cases in Fig. 6 (c). In the first group the recovery was faster more upstream and moderated afterwards, when compared to the FB case. Conversely, in the second group the recovery was moderate first and faster more downstream. The third group's cases disturbed the flow both perpendicularly and in the direction of the flow, and appeared to be somewhat between the prior groups.

https://doi.org/10.5194/wes-2025-264
Preprint. Discussion started: 4 December 2025

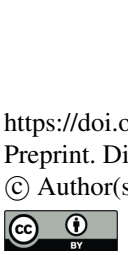

eawe european academy of wind energy
Open Access WIND ENERGY SCIENCE DISCUSSIONS

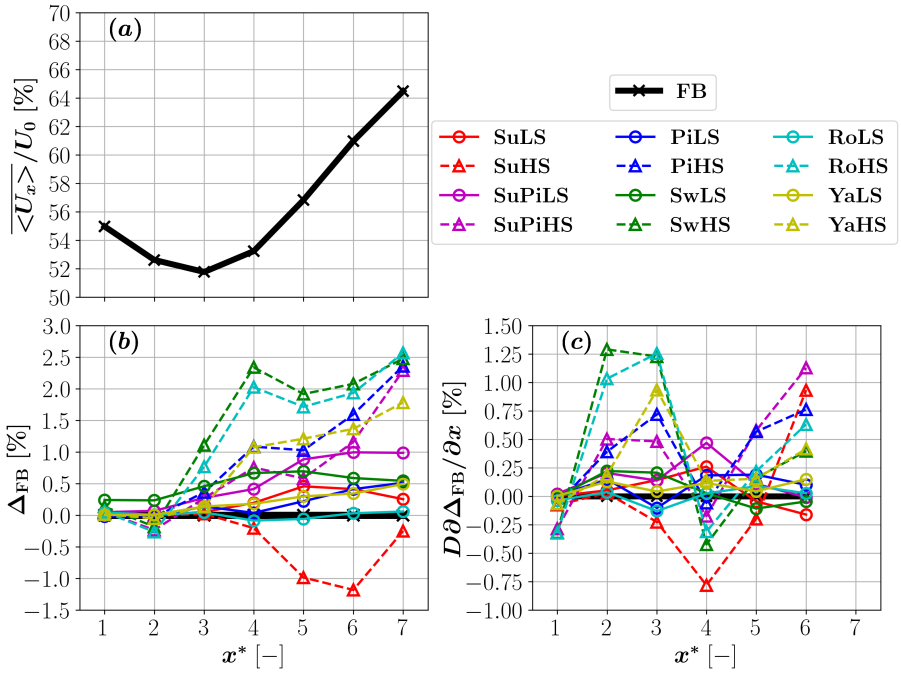

Figure 6. Streamwise evolution of the wake recovery for the FB case (a), wake recovery excess (b) and wake recovery gradient excess (c). Δ_{FB} and $D\partial\Delta_{FB}/\partial x$ are both absolute differences.

The reason for the hampered recovery in SuHS could be explained by analyzing the rotor-centered vertical slices of normalized instantaneous streamwise velocity magnitude U_x/U_0 in Fig. 7, for the FB (a), SuHS (b) and SwHS (c) cases. It is clear that the SuHS case motion in (b) did not lead to noticeable destabilization of the inner jet when compared to the FB case in (a) in the observed region. The SwHS case on the other hand led to a clear destabilization. Moreover, looking at the detail inside the small black rectangle, the structures created by the SuHS motion actually slowed the wake down relative to both the FB and SwHS cases, as seen by the darker shades of blue in (b). Both the lack of destabilization of the inner jet and the velocity field induced by the wake structures appear to be plausible causes of the hampered wake recovery in the SuHS case.

3.2 Turbulence intensity

The second question that was investigated was the effect of the prescribed motion on the turbulence and the eventual connection to the recovery of the wake. With this end, the unidirectional turbulence intensity TI_i was used:

$$TI_i = \frac{<U_i'^2>^{1/2}}{<|U|>}, \tag{7}$$

where $U_i' = U_i - <U_i>$, $i \in \{x, y, z\}$ and $|\cdot|$ denote the vector norm. The streamwise evolution of the streamwise turbulence intensity TI_x can be seen in Fig. 8 for several cases. All floating cases show higher TI_x values, both inside and outside the rotor

https://doi.org/10.5194/wes-2025-264
Preprint. Discussion started: 4 December 2025

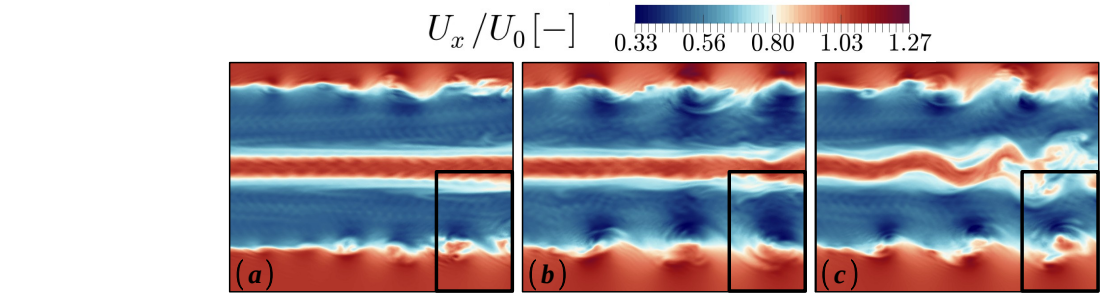

Figure 7. Normalized instantaneous streamwise velocity at the rotor-centered vertical slice for the FB (a), SuHS (b) and SwHS (c) cases. The slices were taken between $x^* = 2$ and $x^* = 4$. The black rectangle highlights differences in the velocity field induced by the wake structures.

area compared to the FB case at $x^* = 2$, and the spread tends to follow the prescribed motion (e.g, higher side-to-side spread for sway), as the near wake still retains its features. Although the wake is not fully turbulent at this stage, higher TI_x values are still an indication of higher perturbations caused by the prescribed motion and a reflection of the level of unsteadiness. Figure 8 further supports the observation of stronger wake destabilization in the high-St/low-A^* cases, that is happening not only at the outer bounds but also in its interior, compared to the FB case. Despite not being shown, the wakes of the low-St/high-A^* cases are very similar to that of the FB case but with higher values of TI_x at the perimeter.

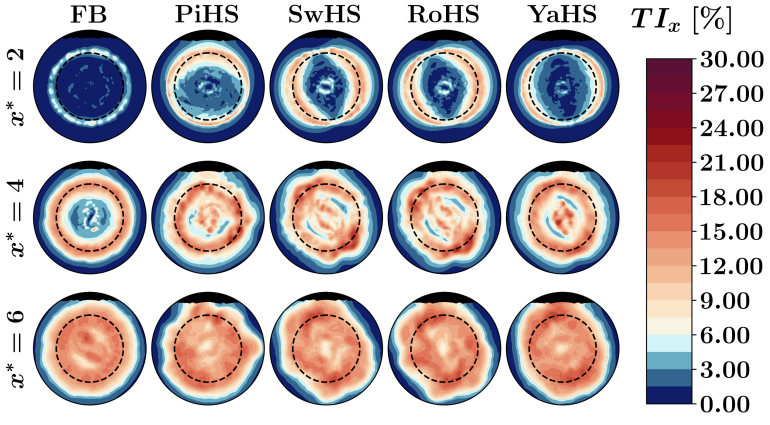

Figure 8. Streamwise turbulence intensity over the radial probes at several downstream positions. The black region corresponds to the upper wall.

Once again, the results were spatially averaged to allow for easier comparison between cases. Figure 9 (a) shows the spatially averaged values of both the streamwise and side-to-side turbulence intensities for the FB case, to show the general trend that the curves take. Both turbulence intensities ramped up along the stream and peaked around $x^* = 6$. Figure 9 (b) and (c) show

https://doi.org/10.5194/wes-2025-264
Preprint. Discussion started: 4 December 2025

eawe european academy of wind energy
Open Access WIND ENERGY SCIENCE DISCUSSIONS

the streamwise and side-to-side turbulence intensities excesses between all cases and the FB case, respectively. The turbulence intensities excesses were calculated with an expression analogous to Eq. (5). Similarly, they are both absolute differences between physical quantities measured in percentage, and hence also measured in percentage. The high-St/low-A^* cases show higher $\overline{TI_x}$ values than the low-St/high-A^* cases between $x^* = 2$ and $x^* = 4$ and vice-versa after $x^* = 5$. The high-St/low-A^* values diverge upwards and converge downwards very quickly towards the FB case values, while the low-St/high-A^* values maintain an almost constant difference until $x^* = 5$, before dropping. For $\overline{TI_y}$, the high-St/low-A^* cases show higher values than the low-St/high-A^* from $x^* = 2$ onward, with peaks between $x^* = 3$ and $x^* = 4$. The trend for the low-St/high-A^* cases is close to that of the fixed-bottom case for this component, except for the SuPiLS case. The results show a link between higher values of wake recovery excess, wake recovery gradient excess (see Fig. 6) and side-to-side turbulence intensity excess until $x^* = 4$. More specifically, higher values of side-to-side turbulence intensity excess were associated with higher wake recovery gradient excesses, with an exception for SuHS. The link makes sense because wake motions in directions perpendicular to the flow increase the contact area with the free stream, thus increasing the potential for momentum entrainment.

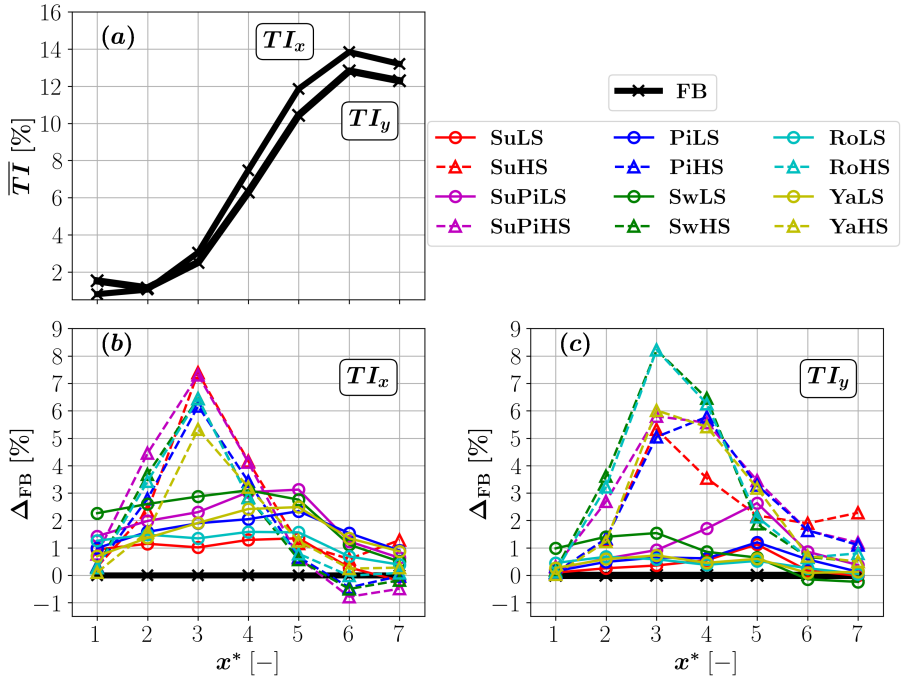

Figure 9. (a) Streamwise evolution of the spatially averaged turbulence intensity in two directions for the FB case; (b) Excess streamwise turbulence intensity due to the prescribed motion; (c) Excess side-to-side turbulence intensity due to the prescribed motion. Δ_{FB} is an absolute difference.

After $x^* = 5$, the SuPiHS $\overline{TI}$ curves converged to those of PiHS. For the SuPiLS, the coupling seemed to have had some degree of coupled effect on the wake, in that the $\overline{TI}$ values of the coupled motion were higher than surge and pitch alone, similarly to what happened with the wake recovery excess.

https://doi.org/10.5194/wes-2025-264
Preprint. Discussion started: 4 December 2025

eawe european academy of wind energy
Open Access WIND ENERGY SCIENCE DISCUSSIONS

3.3 Frequency contents

So far, different prescribed motion directions and $St - A^*$ pairs were linked to different wake recovery excess and TI profiles. Given this link, one should be able to observe differences in how the prescribed motion manifests itself in the wake by analyzing, for instance, the normalized power spectrum of the side-to-side velocity component:

$$\frac{P_{yy}(St)}{{U_0}^2} = \frac{|\widehat{U_y}(t)|^2}{{U_0}^2}, \tag{8}$$

where $\widehat{\cdot}$ denotes the fast Fourier transform (FFT), $|\cdot|$ denotes the complex number modulus and the frequency f was non-dimensionalized into St. For each radial probe, the results were spatially averaged over each probe point inside the rotor perimeter with a simple sample average, leading to the spatially averaged wake spectrum $\overline{P_{yy}}(St)/U_0^2$.

Figure 10 shows the streamwise evolution of this quantity for the FB and both sway cases. The plot indicates that the FB case developed velocity perturbations that concentrated in the range of approximately $0.5 \leq St \leq 1.5$ at $x^* = 4$. At $x^* = 6$, only some reminiscent peaks were found in the range $0.5 \leq St \leq 1$ with a peak at $St = 0.5$. The slope at high frequencies approached minus five-thirds, as expected for freely decaying turbulence at high Re. The peaks identified in the FB case appeared to shift to lower frequencies as the wake progressed downstream. The sway cases, on the other hand, showed peaks at St_p, St_r and their multiples. Moreover, there were peaks at the sum and differences between St_r and St_p and their multiples. This led to a high-energy region in SwLS around the 3P frequency $3St_\mathrm{r} = 3f_\mathrm{r}D/U_0 = 7.14$, among other regions. For SwHS, well-defined sums and differences were present instead of the high-energy region since the prescribed motion frequency and the rotor frequency were much closer. For both sway cases, the prescribed motion frequency was amplified between $x^* = 2$ and $x^* = 4$ and decayed afterwards. At $x^* = 6$, only the prescribed motion frequency showed a strong peak for SwHS, while for SwLS, the magnitude of the prescribed motion frequency peak was closer to that of the peak frequencies in the range of $0.5 \leq St \leq 1$. Although not included in this paper, the spectra of the remaining high-St/low-A^* and low-St/high-A^* cases were very similar to the spectra of SwHS and SwLS, respectively.

The spectra suggested an explanation as to why the high-St/low-A^* cases presented stronger wake perturbations (indicated by higher TI values) than the low-St/high-A^* cases: contrary to the low-St/high-A^* cases, the prescribed frequency in the high-St/low-A^* cases was within the frequency range at which the wake developed velocity perturbations in the fixed-bottom case ($0.5 \leq St \leq 1.5$). This frequency range should represent the natural modes of the wake and exciting those modes should lead to their amplification. The outcome of this would be higher values of the prescribed motion spectral components for the high-St/low-A^* cases, which was indeed what was found. This effect was more clearly observed in the physical quantity described below. First, the spatially averaged normalized velocity amplitude spectrum at the prescribed motion frequency was calculated:

$$\frac{\overline{A_i}(St_\mathrm{p})}{U_0} = \left.\frac{\overline{|\widehat{U_i}(t)|}}{U_0}\right|_{St=St_\mathrm{p}}, \tag{9}$$

https://doi.org/10.5194/wes-2025-264
Preprint. Discussion started: 4 December 2025

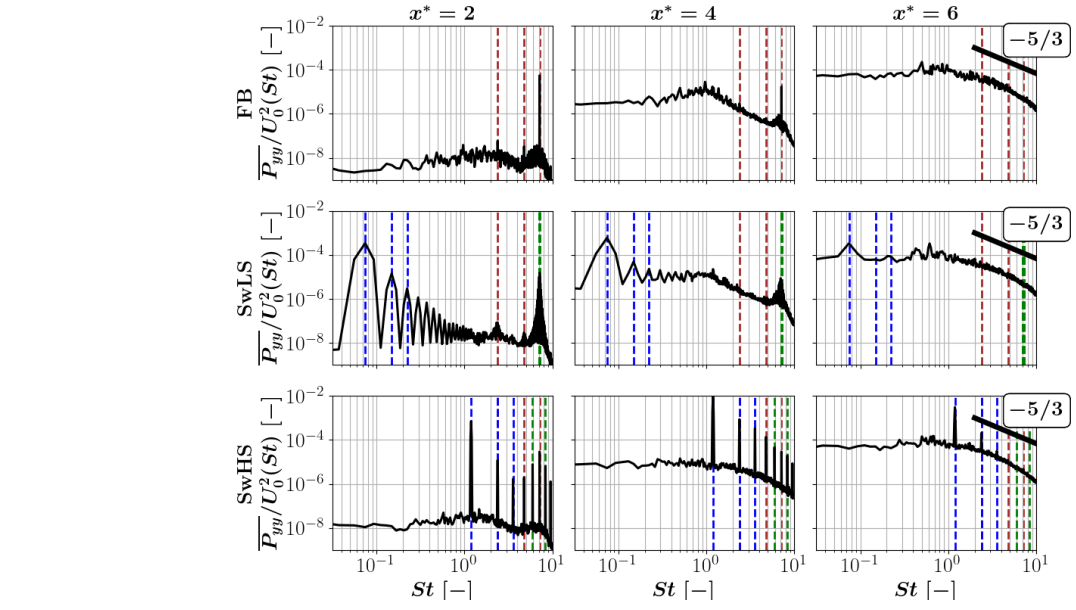

Figure 10. Spatially averaged wake spectra of the side-to-side velocity component. The red lines are the first three multiples of the rotational frequency St_r. The blue lines are the first three multiples of the prescribed motion frequency St_p. The green lines are the sum and difference between $3St_\mathrm{r}$ and St_p.

where i denotes the considered direction. From this, the velocity perturbation amplification factors, which assess the velocity perturbations against the initial prescribed motion perturbation, were defined:

$$k_i(St_\mathrm{p}) = \frac{\overline{A_i}(St_\mathrm{p})}{A_\mathrm{prc}\omega_\mathrm{p}}, \tag{10}$$

where A_prc is the prescribed motion amplitude in the rotor center and ω_p is the prescribed motion angular frequency. This was done because some prescribed motions might have had a stronger presence in the wake simply because the initial perturbation was stronger. In essence, $A_\mathrm{prc}\omega_\mathrm{p}$ represents the prescribed motion velocity amplitude in the rotor center. For yaw, the maximum perturbation velocity was computed at the tip of a blade with an azimuth of $\theta = 90$ deg, assuming a non-rotating rotor. Figure 11 shows the amplification factors of the side-to-side velocity amplitude spectrum at the prescribed motion frequency for all cases with prescribed motion.

Almost all high-St/low-A^* cases showed a sharp increase in amplification factors in the region $2 \leq x^* \leq 3$ that peaked in $3 \leq x^* \leq 5$, especially the yaw, roll, sway and pitch cases. The low-St/high-A^* cases also showed an increase in the amplification factors but much lower than the corresponding high-St/low-A^* case, farther downstream than the previous cases and with subsequent stabilization. The surge cases presented the lowest amplification of the single DOFs, once again suggesting that wake perturbations in the direction of the flow have a more limited amplification potential in the frequencies and amplitudes studied. The surge-pitch coupling was an outlier since summing the surge and pitch perturbations led to a disproportionately

https://doi.org/10.5194/wes-2025-264
Preprint. Discussion started: 4 December 2025

eawe european academy of wind energy
Open Access WIND ENERGY SCIENCE DISCUSSIONS

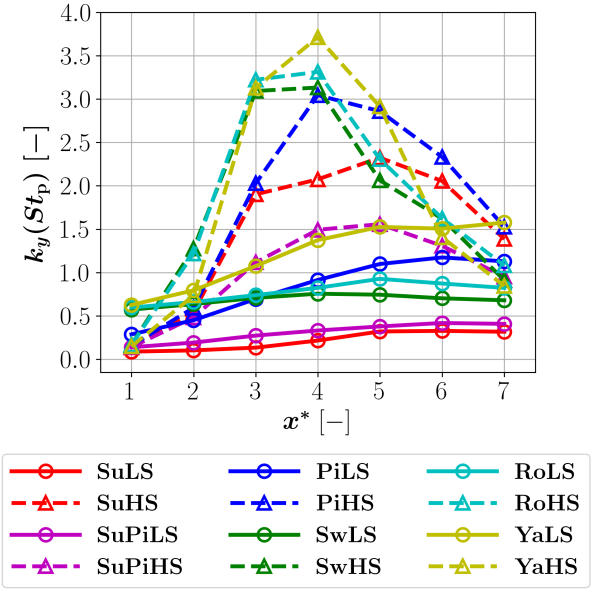

Figure 11. Side-to-side velocity perturbation amplification factors at the prescribed motion frequency. There is no curve for the FB case because there was no prescribed motion.

small increase in $\overline{A_i(St_\mathrm{p})}/U_0$. That is why the amplification factor of the coupled case was lower than those of the single DOFs alone.

These results confirm that the high-St/low-A^* cases amplified the prescribed motion in the wake to a much larger degree than the low-St/high-A^* cases, potentially because the St_p was within the natural modes of the wake. Still, did this amplification happen globally in the wake or at specific regions? This question was answered by observing how $A_y(St_\mathrm{p})/U_0$ was distributed across each wake slice and is shown in Fig. 12. The surge and sway cases are shown in the columns and the streamwise positions are shown in the rows. The white dashed circle indicates the rotor perimeter.

While there was virtually no excitation of the wake for the SuLS and SwLS cases, the contours of the SuHS and SwHS cases indicate that the regions of the wake that were the most excited by the prescribed motion were located at the rotor perimeter and rotor center. This naturally points towards the tip and root vortices and the associated shear layers and, hence, these regions were analyzed in detail in the following sections.

3.4 Tip and root vortex trail

The tip vortices can easily be visualized by plotting the normalized Q-criterion QD^2/U_0^2 that indicates regions where the local rotation is larger than the local strain rate. Figure 13 shows the surface $QD^2/U_0^2 = 2.48$ for the FB (a), SuLS (b), SuHS (c) and SwHS (d) cases, respectively. The SuLS case showed virtually no difference compared to the FB case. The SuHS case, on the other hand, showed a pulsating tip vortex with a larger diameter than the former case which was likely caused by the

https://doi.org/10.5194/wes-2025-264
Preprint. Discussion started: 4 December 2025

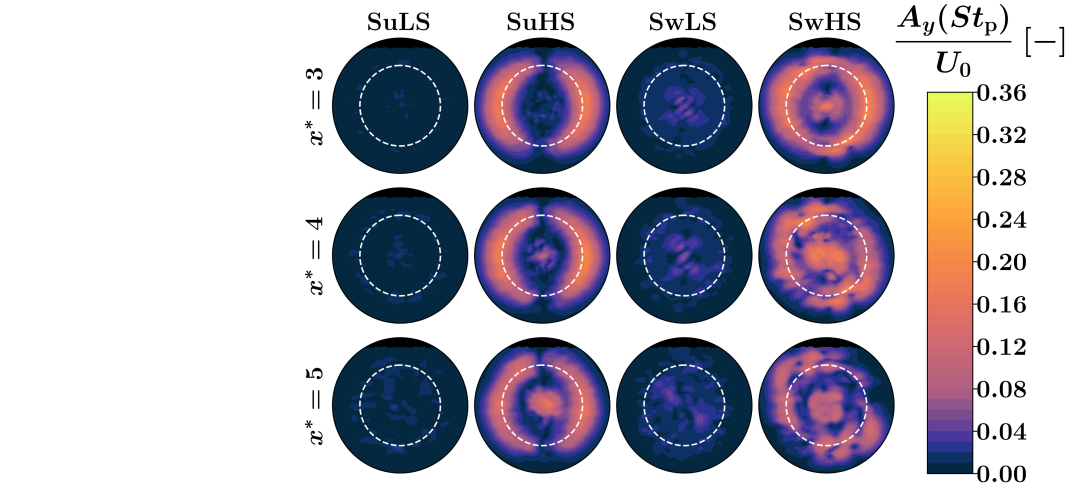

Figure 12. Normalized amplitude spectrum of the side-to-side velocity at the prescribed motion frequency over the radial probes for the surge and sway cases.

earlier onset of the leap-frogging phenomenon followed by the merger between two consecutive tip vortices. These coherent structures were more pronounced and long-lived than in the former cases. In addition to what was observed for SuHS, the SwHS case depicted ripples in the upstream tip vortex envelope and a pulsating vortex that was diagonally deformed. This was consistent with the sway motion direction and appears to have led to the earlier breakdown of the tip vortices with less long-lived structures, when compared with the SuHS case. The phenomena observed both in the SuHS and SwHS cases reinforce the idea that the wake reacted to the prescribed motion and amplified upstream perturbations.

The tip and root vortices were further analyzed by looking at the corresponding trail in some wake slices. The term "trail" was used instead of "shear layer", since defining the shear layer required using more formal methods than the one used in this paper. The tip and root vortex trails were assessed from the normalized standard deviation of the velocity magnitude $<|U|'^2>^{1/2}/U_0$ since both vortices increase the variability of the velocity. This was done at the horizontal domain section slicing the rotor center, i.e. defined by the plane $z^* = z^*_{\mathrm{rc}}$ in Fig. 1 (b), where z^*_{rc} is the normalized rotor center height. Figure 14 shows $<|U|'^2>^{1/2}/U_0$ for the SwLS (a) and SwHS (b) cases, respectively. Both cases are sway cases which means that the turbine was oscillating in the y^* direction. Both contours show two regions of high $<|U|'^2>^{1/2}/U_0$ that emanate from the blade tips and roots and that were consistent with their respective vortices. However, the regions were somewhat different between both cases. In the SwLS case, the tip trail expanded monotonically while the root trail remained almost unchanged. In the SwHS case, the tip trails expanded, contracted and expanded again, leading to a bulb-shaped contour, while the root trails contracted and then expanded.

The trails were delimited in these planes by choosing the value of $<|U|'^2>^{1/2}/U_0$ that would closely conform to the high-$<|U|'^2>^{1/2}/U_0$ region on the SwLS case. The value was $<|U|'^2>^{1/2}/U_0 = 0.044$ and was plotted as a yellow line in Fig. 14.

https://doi.org/10.5194/wes-2025-264
Preprint. Discussion started: 4 December 2025

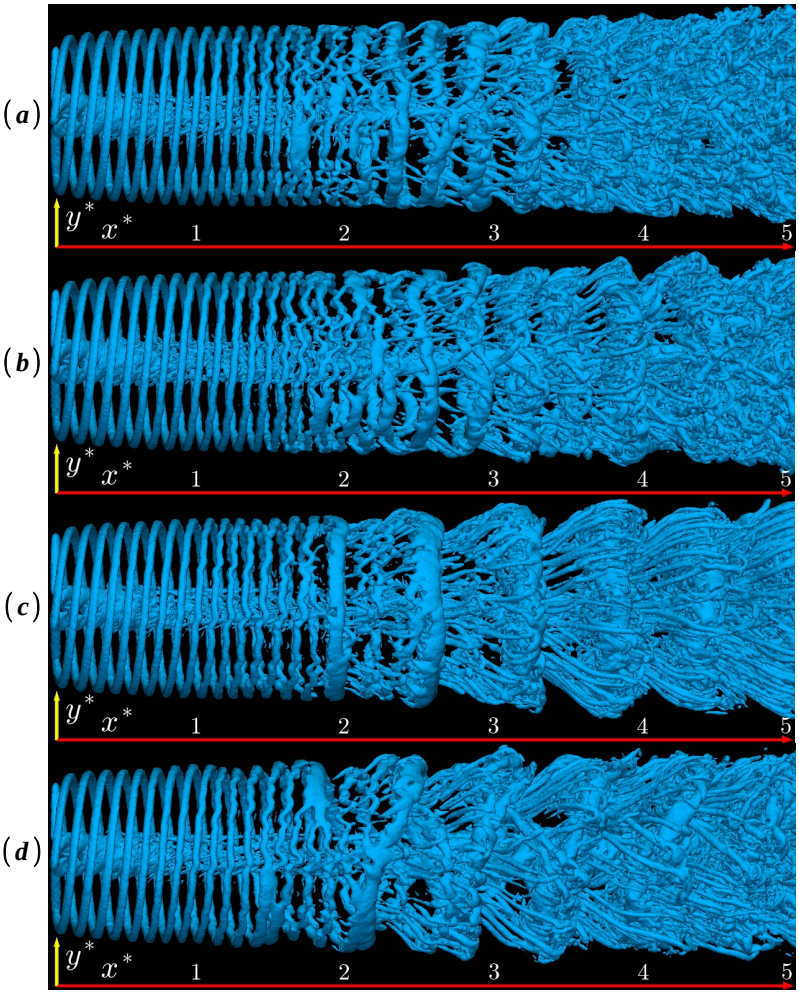

Figure 13. Normalized Q-criterion surface $QD^2/U_0^2 = 2.48$ for the (a) FB, (b) SuLS, (c) SuHS, (d) SwHS cases.

The same value was used to track the trail limits of all cases in order to make them comparable. Figure 15 (a) shows the trail limits from Fig. 14 in the $y^* > y^*_{\mathrm{rc}}$ region, together with those of the fixed-bottom case FB for reference. y^*_{rc} is the normalized y^* coordinate of the rotor center. The red horizontal line indicates the tip position, i.e. $y^* = 0.5$. y^*_1 refers to the limit that is closest to the free stream while y^*_2 refers to the limit that is closest to the wake center. The trail half-thickness $y^*_1 - 0.5$ was computed as the difference between y^*_1 and the tip position, and was used to quantify the trail evolution. Figure 15 (b) shows the tip trail half-thickness for all the cases. It was evident that the trails of the high-St/low-A^* cases grew at a much faster rate than the ones from the low-St/high-A^* and FB cases, until $x^* = 3$. Afterwards, the high-St/low-A^* cases' trails contracted between $3 \leq x^* \leq 5$ and were followed by an expansion, forming an "N" shape. In contrast, the low-St/high-A^* cases's trails grew at a much more constant rate.

https://doi.org/10.5194/wes-2025-264
Preprint. Discussion started: 4 December 2025

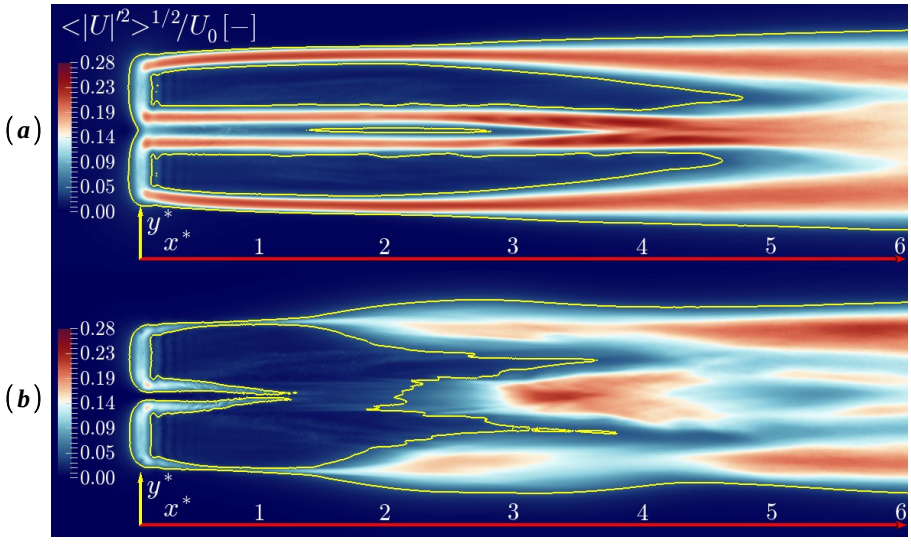

Figure 14. Normalized standard deviation of the velocity magnitude $<|U|'^2>^{1/2}/U_0$ for: (a) the SwLS case, and (b) the SwHS case. The plane is an horizontal domain section slicing the rotor center, i.e. defined by the equation $z^* = z^*_{\mathrm{rc}}$ (see Fig. 1). The reference frame indicates the directions but not the origin.

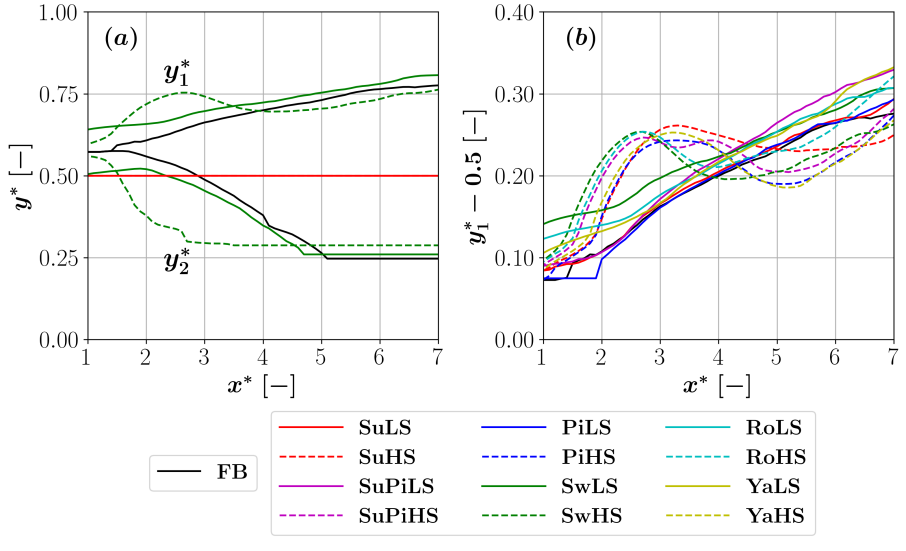

Figure 15. (a) Tip shear layer trails at the $y^* > y^*_{\mathrm{rc}}$ region for the FB, SwLS and SwHS cases. The red line indicates the tip position; (b) Tip shear layer trail half-thickness for all cases.

A necessary condition for the transition to the far-wake is the merger between all tip and root shear layers. Hence, a sooner merger should indicate a sooner transition and a faster recovery. Following this reasoning, the tip and root vortex trail limits

https://doi.org/10.5194/wes-2025-264
Preprint. Discussion started: 4 December 2025

eawe european academy of wind energy
Open Access WIND ENERGY SCIENCE DISCUSSIONS

were used as a proxy for the merger between shear layers, in order to identify differences between the cases. The merger between tip and root vortex trails were identified in the plane shown in Fig. 14 and in the plane $y^* = y^*_{rc}$ which is orthogonal to it and crosses the top and bottom boundaries of the domain. Each plane naturally had two merger points associated with it since there are two pairs of tip and root trails located in opposite sides of the rotor center. The four merger points of all cases were compiled in Figure 16. The low-St/high-A^* cases showed merger points that were very close to those of the FB case,

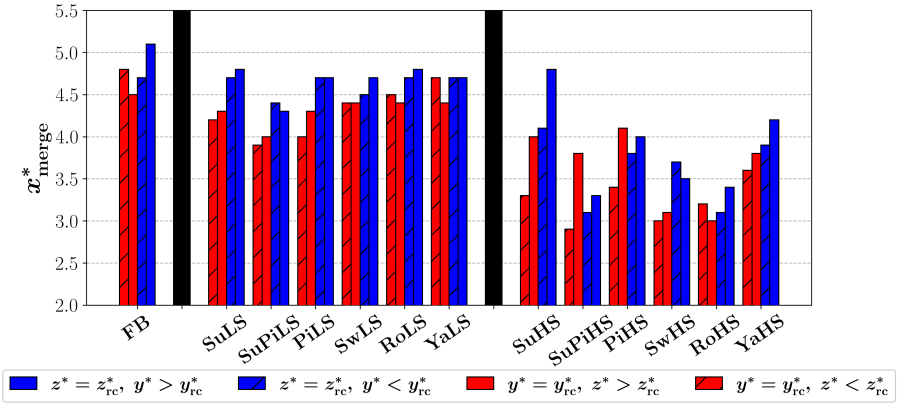

Figure 16. Tip and root trail merger points. The blue bars refer to the merger points in the plane $z^* = z^*_{rc}$ which is the horizontal plane crossing the rotor center. The red bars refer to the merger points in the plane $y^* = y^*_{rc}$ which is the vertical plane crossing the rotor center. Bars with diagonal stripes correspond to positions below the rotor center. Clear bars refer to positions above the rotor center. The black bars separate the cases into the FB case, the low-St/high-A^* cases and the high-St/low-A^* cases.

while the high-St/low-A^* cases clearly showed more upstream merger points. This finding is consistent with the faster wake recovery of the high-St/low-A^* cases and showcases yet another difference between both prescribed motion groups.

Another realization is that the merger points in the plane $y^* = y^*_{rc}$ were almost always located more upstream than those in the plane $z^* = z^*_{rc}$. This was attributed to the reduced height of the domain which might have constrained the flow, thus anticipating the mergers. It is worth highlighting this phenomenon because it is likely to happen in wind tunnels where the blockage ratio is high, such as the POLIMI wind tunnel that was reproduced in the simulations. In spite of this, there is a clear consistency in the results, in that the high-St/low-A^* cases show earlier mergers than the low-St/high-A^* cases, both in the constrained and unconstrained planes. This supports the idea that the floating wind turbine wake phenomena studied in this paper well captured, even under a high blockage ratio conditions.

The last part of this section attempts to link the frequency content of the tip and root regions identified in Fig. 12 to the evolution of the wake trail in Fig. 14. This was done by comparing the evolution of the total trail thickness $y^*_1 - y^*_2$ to the evolution of the amplitude spectrum component at the prescribed motion frequency that was spatially-averaged over the total thickness $\overline{A_y}(St_\mathrm{p})/U_0$, as shown in Fig. 17. The total thickness was used to show that the conclusions applied to the whole trail. For SwLS, it can be seen that the trail expansion was not accompanied by an large increase in $\overline{A_y}(St_\mathrm{p})/U_0$. The same

https://doi.org/10.5194/wes-2025-264
Preprint. Discussion started: 4 December 2025

eawe european academy of wind energy
Open Access WIND ENERGY SCIENCE DISCUSSIONS

was observed for the remaining low-St/high-A^* cases. Conversely, for SwHS and the remaining high-St/low-A^*, there was a sharp increase in $\overline{A_y}(St_\mathrm{p})/U_0$ that peaked approximately at the maximum thickness position, providing evidence that the early trail expansion was triggered by the prescribed motion.

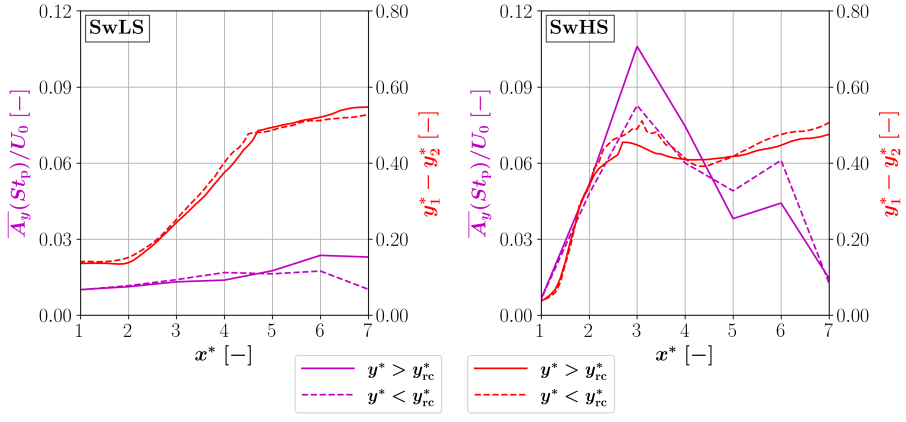

Figure 17. Normalized side-to-side velocity amplitude spectrum at the prescribed motion frequency spatially averaged over the tip total trail thickness for the SwLS and SwHS cases in the plane $z^* = z_\mathrm{rc}^*$ (see Fig. 1).

3.5 Wake meandering

One aspect of the wake that may be relevant for the recovery and downstream turbine load calculation is the wake meandering induced by the prescribed motion. The estimation of the instantaneous wake center described in Appendix D was used to quantify the meandering, which was visualized by spatially binning the instantaneous wake center coordinates at each time instant, in order to obtain their distribution f in space. Figure 18 shows the wake center distribution for the FB, SwLS and SwHS cases in the first, second and third rows. Columns from left to right correspond to a sequence of streamwise positions. The reference frame is centered at the rotor center. The FB case displayed a wake center highly concentrated at the center of the reference frame that started to smear out from $x^* = 5$. The SwLS case, on the other hand, exhibited a highly concentrated side-to-side motion over a horizontal line at $x^* = 1$, consistent with the sway motion. Afterwards, the line rotated and the wake center concentrated at two diametrically opposite positions. Likewise, the line gradually smeared out, until a diffuse pattern was reached at $x^* = 7$, leading to a more isotropic wake meandering that was common to all cases. For SwHS, the results were quite similar to those of the FB case but slightly more diffuse. All in all, these results suggest that the prescribed motion does seem to provoke wake meandering in the directions associated with the prescribed motion.

Using an amplification factor approach similar to the one described in Section 3.3, it was possible to evaluate which cases were more prone to wake meandering. First, the wake center normalized amplitude spectra at the prescribed motion frequency

https://doi.org/10.5194/wes-2025-264
Preprint. Discussion started: 4 December 2025

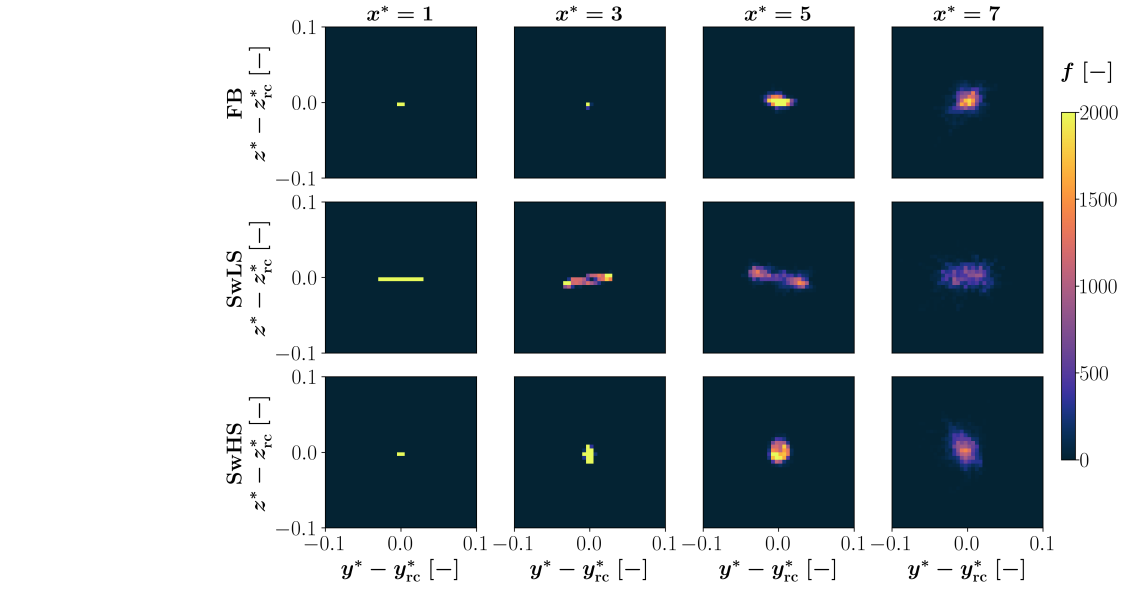

Figure 18. Relative frequency distribution of the wake center f in a reference frame centered at the rotor center.

was used to characterize the meandering intensity, as follows:

$$A^*_{\mathrm{wc}}(St_{\mathrm{p}}) = \sqrt{\frac{A^{*2}_{y_{\mathrm{wc}}}(St_{\mathrm{p}}) + A^{*2}_{z_{\mathrm{wc}}}(St_{\mathrm{p}})}{2}}, \tag{11}$$

where,

$$A^*_{i\,\mathrm{wc}}(St) = |\widehat{x^*_{i\,\mathrm{wc}}}(t)|, \tag{12}$$

is the wake center normalized amplitude spectra at the prescribed motion frequency, i denotes the considered direction, "wc" stands for wake center and the frequency was normalized (St). The wake meandering amplification factors k were then calculated as:

$$k_{\mathrm{wc}}(St_{\mathrm{p}}) = \frac{A^*_{\mathrm{wc}}(St_{\mathrm{p}})}{A^*_{\mathrm{prc}}}. \tag{13}$$

where A^*_{prc} was the prescribed motion amplitude at the rotor center.

Figure 19 shows the amplification factors for all cases with prescribed motion. Similarly to the velocity perturbations in Fig. 11, the high-St/low-A^* cases amplified the prescribed motion more than the low-St/high-A^* cases. Curiously, the amplification factors dipped at $x^* = 6$ and recovered at $x^* = 7$, which suggests a transition to the natural meandering of the wake from the perturbation caused by the prescribed motion. Overall, the meandering intensity peaked between $x^* = 4$ and $x^* = 5$ for all cases, which was more downstream than the velocity perturbations in Fig. 11.

The results presented in this section ("Results") are further analyzed and discussed in the following section ("Discussion"), which also attempts to connect the different aspects of the wake.

https://doi.org/10.5194/wes-2025-264
Preprint. Discussion started: 4 December 2025

eawe european academy of wind energy
Open Access WIND ENERGY SCIENCE DISCUSSIONS

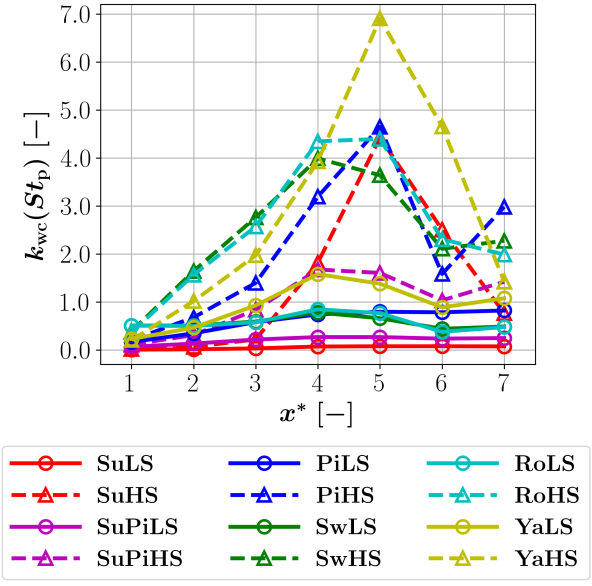

Figure 19. (a) Normalized average amplitude spectra; (b) wake meandering amplification factors.

4 Discussion

In terms of wake recovery, the results suggest that the floating motion is generally beneficial for the wake recovery. Compared to the results in the literature, the recovery onset positions and wake recovery excess trends for the sway cases were similar to the closest simulated St in Li et al. (2022). Despite this, the overall wake recovery excess values were lower than expected. The results of Gupta and Wan (2019) and Li et al. (2022) suggest that this was due to the fact that the values of St were either too low and too high to be in the most favorable range for wake recovery. Regarding the detrimental effect of surge, Messmer et al. (2024) reports a drop in the wake recovery excess in surge when the St goes from 0.81 to 0.97. If the wake recovery excess maintains the trend and keeps on decreasing, it is plausible that there might be a St beyond which the surge motion is actually detrimental to the wake recovery. This detrimental effect was also reported for some sway cases at $St = 0.1$ and $St = 0.8$ in Li et al. (2022).

As for the evolution of the turbulence intensity, all cases generally led to higher values of streamwise turbulence intensity. The high-St/low-A^* cases, in particular, led to pronounced spikes at $x^* = 3$. Similar trends were found for the overall turbulence intensity in sway by Li et al. (2022), for the closest simulated St numbers, namely a more upstream and pronounced TI increase for the highest St numbers. Contrary to the streamwise turbulence intensity, the low-St/high-A^* cases did not show, in general, significant increases in the side-to-side turbulence intensity, unlike the high-St/low-A^* cases. This supports the idea that flow-perpendicular perturbations are more beneficial to the wake recovery.

When it comes to the wake spectra, all floating cases passed the prescribed motion frequency and related frequencies onto the wake. For the fixed-bottom case, the identified peak frequency $St = 0.5$ at $x^* = 6$ was close to those found in the literature

https://doi.org/10.5194/wes-2025-264
Preprint. Discussion started: 4 December 2025

eawe european academy of wind energy
Open Access WIND ENERGY SCIENCE DISCUSSIONS

(Heisel et al., 2018). The wake naturally developed a high energy region in the range of approximately $0.5 \leq St \leq 1.5$ at $x^* = 4$, which could explain why the prescribed frequency of $St = 1.1905$ was amplified by the wake contrary to $St = 0.0744$, looking at this from the perspective of a resonance phenomenon. Until $x^* = 6$, the highest peaks for all cases coincided with the prescribed motion frequency, in accordance with Mao and Sørensen (2018) for the optimally perturbed flow. The velocity perturbation amplification factors at the prescribed motion frequency of all the high-St/low-A^* cases were the highest and showed a sharp increase in the region $2 \leq x^* \leq 3$ that peaked in $3 \leq x^* \leq 5$ and decayed afterwards. This was generally consistent with the highest simulated St in Li et al. (2022) and Messmer et al. (2024). The low-St/high-A^* cases showed lower amplification factors characterized by a less pronounced and continuous increase, that was farther downstream and with subsequent stabilization, similarly to the results for $St = 0.2$ in Li et al. (2022).

At this point, the results suggest a plausible relationship between the wake recovery, turbulence intensity and frequency content in the wake: motions at certain frequency-amplitude pairs perturb the wake more than others, in such as way that these perturbations are amplified and are reflected as higher turbulence intensity. In turn, the larger perturbations, especially those perpendicular to the flow, are likely to improve the mixing with the free stream which would explain the improved recovery. The regions were the amplification took place were found to be the tip and root vortices and the corresponding shear layers, as previously noted by Mao and Sørensen (2018). The Q-criterion contours showed pulsating patterns for the high-St/low-A^* surge case and diagonally-deformed pulsating patterns for the high-St/low-A^* sway case, that were similar to the ones found by Messmer et al. (2024). The patterns for the low-St/high-A^* cases very much the same as the one of the fixed-bottom case.

The analysis of the tip vortex trails revealed an N-shaped evolution of its half-thickness for the high-St/low-A^* cases, where the steep increase between $x^* = 2$ and $x^* = 3$ was accompanied by an also steep increase in the average value of the spectral component of the side-to-side velocity at the prescribed motion frequency along the trail thickness. In contrast, the low-St/high-A^* cases presented a monotonous increase in half-thickness without a material increase in aforementioned spectral component. The tip and root vortex trails merged earlier for the high-St/low-A^* cases. This new cohort of results fits well with the prior results in that the amplification of upstream perturbations at certain frequency-amplitude pairs in the tip and root trails is leading to an earlier wake expansion, which also coincides with the steep increases in TI previously documented. A consequence of this would be earlier mergers between the tip and root vortex trails and a faster wake recovery, which was indeed what was observed for those cases.

Wake meandering patterns were identified that followed the prescribed motion initially but gradually converged to isotropic and dispersed wake meandering at $x^* = 7$. The low-St/high-A^* cases had stronger meandering upstream but the wake meandering amplification factors were still, in general, much higher for the high-St/low-A^* cases. The wake meandering pattern for the low-St/high-A^* sway case was initially linear, rotated with the wake and was concentrated at two diametrically opposite positions, similarly to what was observed by Li et al. (2022). The meandering frequency content was found to be very similar to that of the wake velocity perturbations and the meandering magnitudes at the prescribed motion frequency peaked at $x^* = 5$. This last batch of results links the prescribed motion to enhanced wake meandering that accompanies all the plethora of previously identified wake phenomena.

https://doi.org/10.5194/wes-2025-264
Preprint. Discussion started: 4 December 2025

eawe european academy of wind energy
Open Access WIND ENERGY SCIENCE DISCUSSIONS

Lastly, when it came to the coupling between surge and pitch, some wake characteristics of those cases were closer to the single-DOF pitch motion and some others to the single-DOF surge motion but nothing extraordinary was found in the range of frequencies and amplitudes studied. This could suggest that, at least in these ranges, the upstream perturbation amplitude increase due to the coupling had a very small effect on the wake.

All in all, the simulations performed in this wind tunnel setup with a high blockage ratio capture the wake phenomena induced by the prescribed motion that were found in the literature, except for the wake recovery excess values of the high-St/low-A^* cases, likely due to the very high Strouhal number.

5 Conclusions

This manuscript investigated the wake of a laboratory-scale wind turbine under prescribed motions that covered five degrees-of-freedom and a coupled motion. The values of the prescribed frequencies and amplitudes were chosen to be realistic values for surge and pitch. The same values were used for the remaining analogous degrees-of-freedom so as to provide a fair comparison between cases and to investigate the potential effect of designing for non-realistic values of the remaining DOFs. The simulation setup replicated the POLIMI wind tunnel cross-section with the simultaneous goals of investigating the wake dynamics and checking if it would be materially different under a high blockage ratio. The turbine was operated in the vicinity of rated conditions, under steady and uniform inflow and constant rotor speed in order to highlight the effects of the prescribed motion on the wake evolution.

The results highlighted clear differences between prescribing motions at two different pairs of Strouhal number St and normalized amplitude A^*. The low-St/high-A^* cases exhibited a behavior that was relatively close to the fixed-bottom case. By contrast, the high-St/low-A^* cases presented with more irregular wake boundaries, a faster recovery than the fixed-bottom case, prescribed motion-induced coherent structures in the wake, faster tip and root vortex trail expansion and stronger meandering amplification. This contrast was demonstrated to be caused by the prescribed motion itself whose upstream perturbations were amplified by the wake as it progressed downstream. In particular, the simulated high St was in the high energy region that was naturally developed by the wake of the fixed-bottom case whereas the low St was not, suggesting a resonance phenomenon as the root cause of the differences. The upstream perturbation amplification happened especially at the tip and root trails and was accompanied by faster expansion of the tip vortex trail. This in turn, led to earlier mergers between the tip and root vortex trails, in accordance with the observed faster wake recovery. An outlier in the high-St/low-A^* cases was the surge case that showed a slower wake recovery than the fixed-bottom case, a phenomenon that was linked to its pulsating wake structures. The prescribed motions also caused wake meandering, whose spectra were similar to the wake spectra, despite not being shown. The meandering was most amplified in the high-St/low-A^* cases. Furthermore, the impact of prescribed motions with a component perpendicular to the flow was found to be larger than that of motions exclusively in the flow direction. No extraordinary phenomena were found from coupling surge to pitch, when compared the corresponding single-DOF motions.

https://doi.org/10.5194/wes-2025-264
Preprint. Discussion started: 4 December 2025

eawe european academy of wind energy
Open Access WIND ENERGY SCIENCE DISCUSSIONS

Performing the simulations in this wind tunnel led to high-blockage-ratio conditions and led the wake to interact with the top wall of the setup. Despite this, the conclusions were still in accordance to those found in the literature, supporting the idea that the floating turbine wake dynamics was not significantly affected by the setup.

Appendix A: Prescribed motion validation

The prescribed motion implementation was validated against the theoretical solution of the motion of one point in one of the blades. Deriving the solution involved describing the rotor center coordinates as a function of the prescribed motion and then summing the blade point motion relative to the rotor center due to rotation. Under prescribed translation, the variation in the coordinates of all the turbine points due to the prescribed motion is exactly the same as the prescribed motion affecting those coordinates. Under prescribed rotation, the points on the turbine experience a variation in coordinates that is proportional to the distance to the rotation axis. Recalling the prescribed motion expression in Eq. (2), the sign was negative for translation and positive for rotation, in accordance to Bergua et al. (2023). The coordinates in time for an arbitrary point in the blade on the reference frame $\boldsymbol{e_x}$-$\boldsymbol{e_y}$-$\boldsymbol{e_z}$ (see Fig. 1), with an initial azimuth of $\theta_0 = 0$ deg are shown in Table A1, where $\theta = \omega_\mathrm{r} t$ is the azimuth of a point on the blade; $\omega_\mathrm{r} = 2\pi f_\mathrm{r}$ is the angular frequency of the rotor; t is the time; R is the point's radial position relative to the rotor center; $L_\mathrm{e} = \sqrt{L_1^2 + L_2^2}$ is the distance from the rotor center to the pitch axis (where "e" stands for effective) and $\alpha_\mathrm{e} = \tan^{-1}(L2/L1)$ is the effective angle between the rotor center and the vertical direction. The rotor azimuth angle θ was defined as the azimuth of the blade that is upward pointing at the start of the simulation, i.e., the blade with $\theta_0 = 0$ deg.

Table A1. Blade point coordinates under single-DOF prescribed motion.

DOF	Surge	Sway	Heave	Roll	Pitch	Yaw
$x(t)$	p	0	0	0	$L_2 + L_\mathrm{e}\sin(p - \alpha_\mathrm{e}) + R\sin(p)\cos(\theta)$	$R\sin(\theta)\sin(p) + L_2(1 - \cos(p))$
$y(t)$	$-R\sin(\theta)$	$p - R\sin(\theta)$	$-R\sin(\theta)$	$-L_1\sin(p) - R\sin(\theta + p)$	$-R\sin(\theta)$	$-R\sin(\theta)\cos(p) - L_2\sin(p)$
$z(t)$	$z_\mathrm{rc} + R\cos(\theta)$	$z_\mathrm{rc} + R\cos(\theta)$	$p + z_\mathrm{rc} + R\cos(\theta)$	$z_\mathrm{p} + L_1\cos(p) + R\cos(\theta + p)$	$z_\mathrm{p} + L_\mathrm{e}\cos(p - \alpha_\mathrm{e}) + R\cos(p)\cos(\theta)$	$z_\mathrm{rc} + R\sin(\theta)$

The validation was performed by comparing the normalized displacement calculated with the above expressions with the actual value from the simulations, by means of an error parameter. The normalized displacement Δx_i^* was defined as:

$$\Delta x_i^* = \frac{\Delta x_i}{L_\mathrm{b}} = \frac{x_i(t) - x_{i0}}{L_\mathrm{b}}, \tag{A1}$$

https://doi.org/10.5194/wes-2025-264
Preprint. Discussion started: 4 December 2025

eawe european academy of wind energy
Open Access WIND ENERGY SCIENCE DISCUSSIONS

where i is the direction, L_b is the blade length and x_{i0} is the initial value of the coordinate x_i. The normalized displacement indicates how much the coordinate changed relative to the blade length. The relative error ϵ was defined as follows:

$$\epsilon = \frac{\Delta x_i|_\mathrm{sim} - \Delta x_i|_\mathrm{theo}}{A_\mathrm{pb}}, \tag{A2}$$

where $\Delta x_i|_\mathrm{sim}$ is the simulation displacement, $\Delta x_i|_\mathrm{sim}$ is the theoretical displacement and A_pb is equal to the blade point motion amplitude caused by the prescribed motion exclusively, i.e. with the rotor still. This way, the motion prescription error was measured relative to the prescribed amplitude. The blade point motion amplitudes are summarized in Table A2. For surge, sway and heave, they are simply the prescribed motion amplitude. For roll and pitch, they represent the motion amplitude (in length units) of a blade point at radial distance R from the rotor center and $\theta(t) = 0$ deg (assuming the rotor is not rotating). For yaw, the same is true but assuming $\theta(t) = 90$ deg. The comparison was done for the point at $82\,\%$ of the span with an initial azimuth of 0 deg.

Table A2. Blade point motion amplitude caused by the prescribed motion exclusively.

Cases	Surge	Sway	Heave	Roll	Pitch	Yaw
A_pb	A_p	A_p	A_p	$A_\mathrm{p}(L_1 + R)$	$A_\mathrm{p}\sqrt{(L_1+R)^2 + L_2^2}$	$A_\mathrm{p}\sqrt{L_2^2 + R^2}$

Figure A1 compares the theoretical and simulation coordinate values for the PiLS, PiHS, SwHS and YaHS cases. Both rows represent the coordinates affected by the prescribed motion (e.g. x and z for pitch). Each column represents one case. It can be seen that the prescribed motion closely follows the theoretical prediction, which is something that happened for all cases. The last three cases showed the largest errors of all cases. Although not completely shown, all the low-St/high-A^* cases showed an error very close to 0%. The largest errors occurred for the high-St/low-A^* cases but they were nevertheless below 5% of the prescribed motion at the given point. This small mismatch can be explained by the fact that the prescribed motion is obtained through velocity prescription which leads to integration errors and some lag. We support this argument by noting that the errors were larger when the slope of the curves was higher, i.e, when the coordinate velocity was higher. In length units, these errors were below 0.5 mm which was marginal.

https://doi.org/10.5194/wes-2025-264
Preprint. Discussion started: 4 December 2025

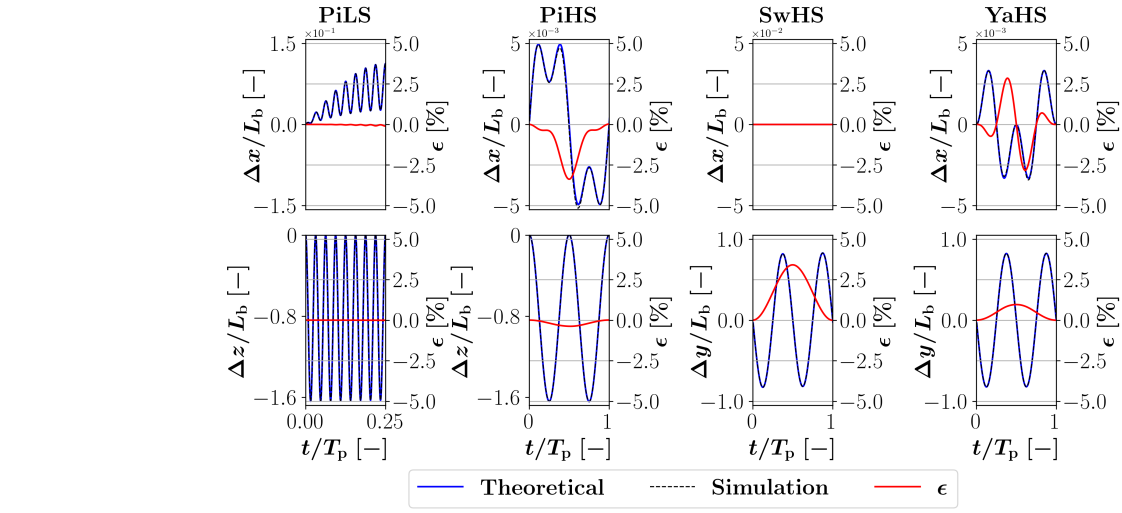

Figure A1. Difference between theoretical prediction of blade point motion and the simulation output. The time was normalized by the prescribed motion period $T_\mathrm{p} = 1/f_\mathrm{p}$.

Appendix B: Flow field convergence

The flow field time convergence was assessed with the forward-moving average of the normalized streamwise velocity component U_x/U_0, defined by:

$$\frac{< U_x >}{U_0}(t) = \frac{< U_x > |_t^{t+\Delta t}}{U_0} \tag{B1}$$

and the forward-moving standard deviation, defined by:

$$\frac{< U_x'^2 >^{1/2}}{U_0}(t) = \frac{< U_x'^2 >^{1/2} |_t^{t+\Delta t}}{U_0}\,, \tag{B2}$$

where $< \cdot >$ denotes the time average performed in the interval $[t, t+\Delta t]$, and $U_x' = U_x - < U_x >$. The simulations were performed for a period of time $T_\mathrm{sim} = 64$ s such that the flow ran through the inlet until the end of the wake refinement region 8.6 times. This time interval was also equal to eight periods of the lowest simulated frequency ($T_{sim} = 8 \times 1/0.125$ s). The distance from the inlet to the end of the wake refinement region was equal to $12.5D$. The averaging time interval Δt was equal to one prescribed motion period.

Figure B1 shows U_x/U_0 in black, $< U_x >/U_0\,(t)$ in blue and $< U_x'^2 >^{1/2}/U_0\,(t)$ in green for the case SwLS. The first and second rows represent the azimuth position of $\theta = 0$ deg and radial positions $r^* = 0$ and $r^* = 1/2$ relative to the rotor center, respectively. Each column stands for a streamwise location. The SwLS case showed reasonable convergence of the statistics at $t_\mathrm{conv} = 4T_\mathrm{p} = 32$ s (red dashed line). Although not shown here, all cases showed similar convergence plots and were deemed converged at $t_\mathrm{conv} = 32$s. Therefore, the time interval from 32 s to 64s, was used for computing the statistics shown in the main body of this manuscript.

https://doi.org/10.5194/wes-2025-264
Preprint. Discussion started: 4 December 2025

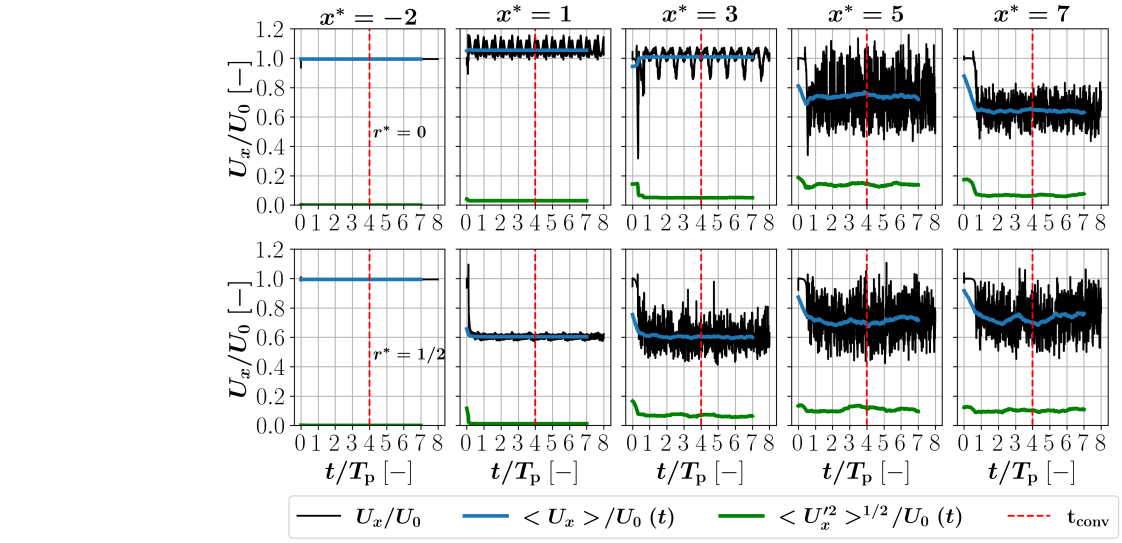

Figure B1. Streamwise flow velocity convergence for SwLf.

Appendix C: Experimental comparison

Some cases were compared to the experimental data available in Bergua et al. (2023); Cioni et al. (2023); Fontanella et al. (2021a, b). An extensive comparison between these experimental data and the results of many participants was carried out with a focus on the loads in Bergua et al. (2023) and a focus on the wake in Cioni et al. (2023). Wake results for a setup similar to the one used in this paper are included in Cioni et al. (2023).

This appendix compares the rotor loads of cases FB, SuLS, SuHS, PiLS and PiHS against the experimental data. Two experiments were performed: Experiment 1 covered the surge cases, and Experiment 2 repeated the surge cases, while adding the pitch cases. In general, experiment 1 showed less variation in the mean aerodynamic forces, indicating more reliable results (Bergua et al., 2023). Experiment 2 may have had some interference due to: the use of a different rotor speed controller that resulted in some rotor speed oscillations; influence of the cable bundle used for the sensors and power located behind the wind turbine; a small blade pitch angle offset (Bergua et al., 2023). Hence, cases FB, SuLS and SuHS come from Experiment 1, while the remaining cases come from Experiment 2. The cases at 2 Hz (SuHS and PiHS), were reported to have higher uncertainty in the measurements associated with the inertial loads and should be evaluated cautiously (Bergua et al., 2023).

The comparison was made in terms of mean value, amplitude of oscillation and phase shift. For the experimental cases, the mean value was taken over the full length of the time series. The amplitude and phase shift were obtained from the FFT spectrum of a section of the time series. This section was the largest section possible such that the frequency step was a submultiple of the prescribed motion frequency. This fact together with the use of a flat-top window reduced spectral leakage and provided the highest amplitude accuracy. The simulation data was post-processed in the same way as the experimental data, from $t = 32$ s to $t = 64$ s.

https://doi.org/10.5194/wes-2025-264
Preprint. Discussion started: 4 December 2025

eawe european academy of wind energy
Open Access WIND ENERGY SCIENCE DISCUSSIONS

C1 Results

Fig. C1 shows the thrust T (top row) and torque M (bottom row) comparisons. The first column addresses the mean load value (denoted by $\overline{\ }$), the second column addresses the amplitude of oscillation (denoted by $'$) and the third column addresses the phase shift between the prescribed motion and the load $\phi_{\mathrm{p}} - \phi_{\mathrm{Load}}$. The difference relative to the experimental value is denoted by $|\Delta|$. Looking at the comparison, in terms of mean value, the simulations differed from the experimental results, at most, 8% and 13% for thrust and torque, respectively. Worse results for torque were potentially expected, since the turbine was designed to match the C_T curve, not the C_P curve. Differences in the load amplitudes for the SuLS and PiLS cases were below 10% and they were somehow expected since the amplitude of variation should scale with the mean value, according to the quasi-steady theory (Fontanella et al., 2021b, 2022). Therefore, some of the error in the amplitude of variation should be related to the error in the mean value. The larger mismatch in the SuHS and PiHS cases was attributed to the higher uncertainty in the measurements associated with the inertial loads. Moreover, the amplitude in the experimental data of PiHS (0.26 deg) was about 13.3% lower than in the load case definition (0.3 deg). As for the phase difference between the motion and the force, there was a reasonable agreement between the simulation and the experimental results.

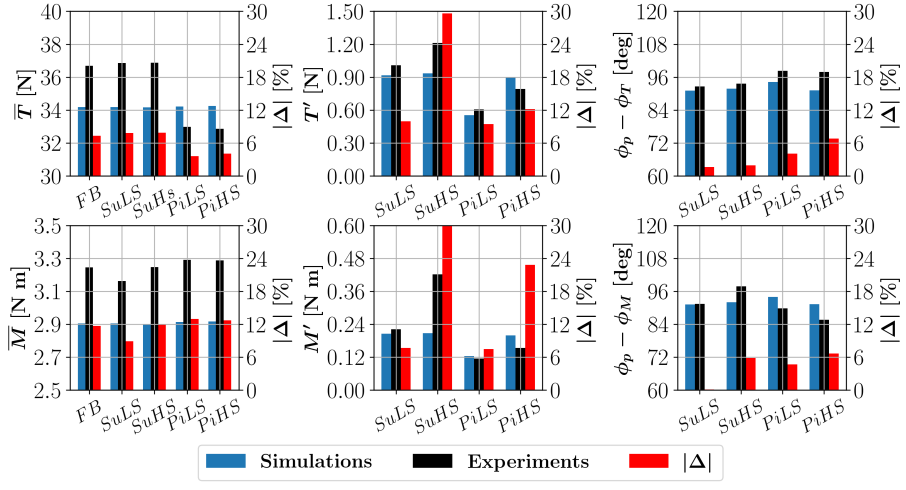

Figure C1. Thrust and torque comparison between simulations and UNAFLOW experiments.

C2 Discussion

Differences between the simulation setup and the experiments include: modeling the mean inflow as uniform, while it was not exactly but almost uniform in the rotor area; the lack of turbulence in the simulations, while the inflow had a 2% turbulence intensity; and modeling the walls as slip walls with no boundary layer. The authors recognize that the simulation setup did not exactly match the experimental setup but would like to mention that there were some difficulties in the experiments that may have exacerbated the mismatches. In terms of the simulations, the most important factor impacting the mismatch was arguably

https://doi.org/10.5194/wes-2025-264
Preprint. Discussion started: 4 December 2025

eawe european academy of wind energy
Open Access WIND ENERGY SCIENCE DISCUSSIONS

the high sensitivity that the actuator-line model has to the smearing length scale ϵ and the cell size Δx, as small changes in these parameters can lead to large changes in the loads. This has been vastly reported in the literature (Mikkelsen, 2003; Troldborg et al., 2009; Martínez-Tossas et al., 2015, 2017; Amaral et al., 2024) and can be overcome by implementing model corrections (Meyer Forsting et al., 2019; Martínez-Tossas and Meneveau, 2019). However, due to time restrictions, it was not possible to explore the topic further and a uniform value of $\epsilon/\Delta x = 2$ (Troldborg et al., 2009) was used.

Appendix D: Instantaneous wake center

At every time step, a Gaussian profile was fit on the streamwise velocity component at each azimuth position of each radial probe. An example of the Gaussian fit (GF) can be seen in Fig. D1. The fit was performed by neglecting the flow velocity values outside the domain and instead replacing them with the last value inside the domain. This was done to ensure that the fit was performed across the same radial distance for all directions, both fully or partially contained in the domain. The fact that the velocity minima were observed away from the centerline is due to the absence of the nacelle in the simulations. For this reason, the fit was performed for each azimuth independently, because fitting the whole wake or diametrically opposed azimuth angles altogether, would have required fitting two Gaussian profiles simultaneously instead of just one. Besides this, fitting azimuthally constrains the fit less, allowing to better capture eventual wake meandering and deformation. Following the

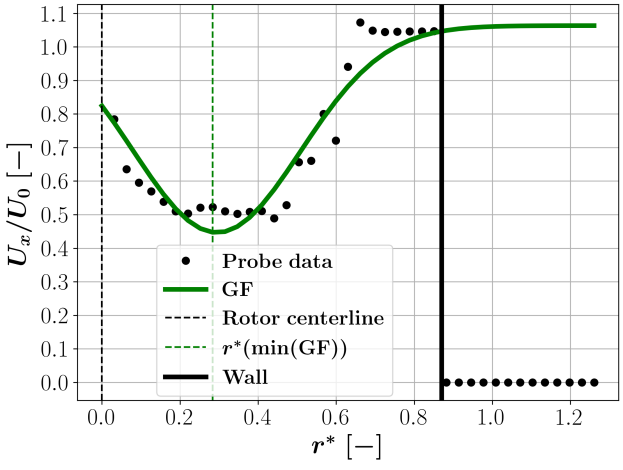

Figure D1. Radial probe streamwise velocity at $x^* = 5$ and $\theta = -33$ deg for case SwLS.

fit, the instantaneous center coordinates were calculated as the average between the fit minima over all the azimuth angles:

$$x^*_{i\,\mathrm{wc}} = \frac{1}{98}\sum_{n=1}^{98} x^*_i(\min(\mathrm{GF}(\theta_n))), \tag{D1}$$

where i denotes the considered direction and θ_n is the azimuth angle of the probe n.

https://doi.org/10.5194/wes-2025-264
Preprint. Discussion started: 4 December 2025

eawe european academy of wind energy
Open Access WIND ENERGY SCIENCE DISCUSSIONS

Data availability. All simulation data are available upon request. Commercial licenses for YALES2 can be purchased from Laboratoire CORIA.

Author contributions. RA performed the simulations, post-processing and was responsible for writing the paper. FHM provided indispensable support in handling the simulation tool, provided text excerpts, references and some figures. All the authors provided valuable input and insights that were important to steer the work and write the paper. PD and AV were crucial in providing the necessary resources to produce this work.

Competing interests. RA, DvT and AV declare that they have no conflict of interest. FHM, KL and PD declare that they were full-time employees of Siemens Gamesa Renewable Energy at the time this work was carried out.

Acknowledgements. This work results from the STEP4WIND project, a European Doctorate programme granted under the H2020 Marie-Curie Innovative Training Network (H2020-MSCA-ITN-2019, grant 860737.) We thank SURF (www.surf.nl) for the use of the National Supercomputer Snellius. This work is part of W2ITASEC (Wind turbine Wake Interactions through Aero-Servo-Elastic Coupling) with computer resources provided by GENCI at TGCC (grant 2023-S142aspe00038 on the supercomputer Joliot Curie). We would like to thank Roger Bergua and Alessandro Fontanella for providing information regarding the experimental setup used to benchmark the simulations.

https://doi.org/10.5194/wes-2025-264
Preprint. Discussion started: 4 December 2025

eawe european academy of wind energy
Open Access WIND ENERGY SCIENCE DISCUSSIONS

References

Ainslie, J. F.: Calculating the flowfield in the wake of wind turbines, Journal of Wind Engineering and Industrial Aerodynamics, 27, 213–224, 1988.

Amaral, R., Houtin-Mongrolle, F., von Terzi, D., and Viré, A.: Nacelle modeling considerations for wind turbines using large-eddy simulations, J. Phys.: Conf. Ser., 2767, https://doi.org/10.1088/1742-6596/2767/5/052056, 2024.

Bak, C., Zahle, F., Bitsche, R., Kim, T., Yde, A., Henriksen, L. C., Hansen, M. H., Blasques, J. P., Gaunaa, M., and Natarajan, A.: The DTU 10-MW reference wind turbine, Tech. rep., Danish Wind Power Research, available at: http://orbit.dtu.dk/files/55645274/The_DTU_10MW_Reference_Turbine_Christian_Bak.pdf, 2013.

Barooni, M., Ashuri, T., Velioglu Sogut, D., Wood, S., , and Ghaderpour Taleghani, S.: Floating Offshore Wind Turbines: Current Status and Future Prospects, Energies, 16, https://doi.org/10.3390/en16010002, 2023.

Bastankhah, M. and Porté-Agel, F.: A new analytical model for wind-turbine wakes, Renew. Energy, 70, 116–123, https://doi.org/10.1016/j.renene.2014.01.002, 2014.

Bayati, I., Belloli, M., Bernini, L., and Zasso, A.: Aerodynamic design methodology for wind tunnel tests of wind turbine rotors, Journal of Wind Engineering and Industrial Aerodynamics, 167, 217–227, https://doi.org/10.1016/j.jweia.2017.05.004, 2017.

Benard, P., Viré, A., Moureau, V., Lartigue, G., Beaudet, L., Deglaire, P., and Bricteux, L.: Large-Eddy Simulation of wind turbines wakes including geometrical effects, Computers and Fluids, 173, 133–139, https://doi.org/10.1016/j.compfluid.2018.03.015, 2018.

Bergua, R., Robertson, A., Jonkman, J., Branlard, E., Fontanella, A., Belloli, M., Schito, P., Zasso, A., Persico, G., Sanvito, A., Amet, E., Brun, C., Campaña-Alonso, G., Martín-San-Román, R., Cai, R., Cai, J., Qian, Q., Maoshi, W., Beardsell, A., Pirrung, G., Ramos-García, N., Shi, W., Fu, J., Corniglion, R., Lovera, A., Galván, J., Nygaard, T. A., dos Santos, C. R., Gilbert, P., Joulin, P.-A., Blondel, F., Frickel, E., Chen, P., Hu, Z., Boisard, R., Yil-mazlar, K., Croce, A., Harnois, V., Zhang, L., Li, Y., Aristondo, A., Mendikoa Alonso, I., Mancini, S., Boorsma, K., Savenije, F., Marten, D., Soto-Valle, R., Schulz, C. W., Netzband, S., Bianchini, A., Papi, F., Cioni, S., Trubat, P., Alarcon, D., Molins, C., Cormier, M., Brüker, K., Lutz, T., Xiao, Q., Deng, Z., Haudin, F., , and Goveas, A.: OC6 project Phase III: validation of the aerodynamic loading on a wind turbine rotor undergoing large motion caused by a floating support structure, Wind Energ. Sci., 8, 465–485, https://doi.org/10.5194/wes-8-465-2023, 2023.

Chamorro, L. P. and Porté-Agel, F.: Effects of thermal stability and incoming boundary-layer flow characteristics on wind-turbine wakes: a wind-tunnel study, Bound.-Lay. Meteorol., 136, 515-533, https://doi.org/10.1007/s10546-010-9512-1, 2010.

Chamorro, L. P., Hill, C., Morton, S., Ellis, C., Arndt, R. E. A., and F, S.: On the interaction between a turbulent open channel flow and an axial-flow turbine, J. Fluid Mech., 716, 658-670, https://doi.org/10.1017/jfm.2012.571, 2013.

Cioni, S., Papi, F., Pagamonci, L., Bianchini, A., Ramos-García, N., Pirrung, G., Corniglion, R., Lovera, A., Galván, J., Boisard, R., Fontanella, A., Schito, P., Zasso, A., Belloli, M., Sanvito, A., Persico, G., Zhang, L., Li, Y., Zhou, Y., Mancini, S., Boorsma, K., Amaral, R., Viré, A., Schulz, C. W., Netzband, S., Soto-Valle, R., Marten, D., Martín-San-Román, R., Trubat, P., Molins, C., Bergua, R., Branlard, E., Jonkman, J., , and Robertson, A.: On the characteristics of the wake of a wind turbine undergoing large motions caused by a floating structure: an insight based on experiments and multi-fidelity simulations from the OC6 project Phase III, Wind Energ. Sci., 8, 1659–1691, https://doi.org/10.5194/wes-8-1659-2023, 2023.

Costanzo, G., Brindley, G., O'Sullivan, R., de Velde, L. V., and Bickley, J.: Latest wind energy data for Europe: Autumn 2024, Tech. rep., Wind Europe, available at: https://windeurope.org/intelligence-platform/product/latest-wind-energy-data-for-europe-autumn-2024/#overview, 2024.

https://doi.org/10.5194/wes-2025-264
Preprint. Discussion started: 4 December 2025

Cozzi, L., Wanner, B., Donovan, C., Toril, A., Yu, W., Arsalane, Y., D'Ambrosio, D., Liu, J., Papapanagiotou, S., Pavarini, C., Perugia, D., Staas, L., Waldron, M., Gould, T., Hosker, E., Justus, D., Coon, T., Santos, M. D., and Tsoukala, E.: Offshore Wind Outlook 2019, World Energy Outlook Special Report, Tech. rep., International Energy Agency, available at: https://www.iea.org/reports/offshore-wind-outlook-2019, 2019.

De Cillis, G., Cherubini, S., Semeraro, O., Leonardi, S., and De Palma, P.: POD-based analysis of a wind turbine wake under the influence of tower and nacelle, Wind Energ., 24, 609–633, https://doi.org/10.1002/we.2592, 2020.

Fontanella, A., Bayati, I., Mikkelsen, R., Belloli, M., and Zasso, A.: UNAFLOW: UNsteady Aerodynamics of FLOating Wind turbines, Zenodo [data set], 173, 133–139, https://doi.org/10.5281/zenodo.4740006, 2021a.

Fontanella, A., Bayati, I., Mikkelsen, R., Belloli, M., and Zasso, A.: UNAFLOW: a holistic wind tunnel experiment about the aerodynamic response of floating wind turbines under imposed surge motion, Wind Energ. Sci., 6, 1169–1190, https://doi.org/10.5194/wes-6-1169-2021, 2021b.

Fontanella, A., Facchinetti, A., Di Carlo, S., and Belloli, M.: Wind tunnel investigation of the aerodynamic response of two 15 MW floating wind turbines, Wind Energy Science Discussions, 2022, 1–25, 2022.

Gambuzza, S. and Ganapathisubramani, B.: The influence of free stream turbulence on the development of a wind turbine wake, J. Fluid Mech., 963, https://doi.org/10.1017/jfm.2023.302, 2023.

Germano, M., Piomelli, U., Moin, P., and Cabot, W. H.: A dynamic subgrid-scale eddy viscosity model, Phys. Fluids, 3, 1760–1765, https://doi.org/10.1063/1.857955, 1990.

Gupta, V. and Wan, M.: Low-order modelling of wake meandering behind turbines, Journal of Fluid Mechanics, 877, 534–560, 2019.

Heisel, M., Hong, J., and Guala, M.: The spectral signature of wind turbine wake meandering: A wind tunnel and field-scale study, Wind Energy, 21, 683–806, https://doi.org/10.1002/we.2189, 2018.

Hodgson, E. L., Madsen, M. H. A., and Andersen, S. J.: Effects of turbulent inflow time scales on wind turbine wake behavior and recovery, Physics of Fluids, 35, 2023.

Houtin-Mongrolle, F.: Investigations of yawed offshore wind turbine interactions through aero-servo-elastic Large Eddy Simulations, Ph.D. thesis, INSA Rouen Normandie, https://theses.hal.science/tel-03987411v1/document, 2022.

Howard, K. B., Singh, A., F, S., and Guala, M.: On the statistics of wind turbine wake meandering: an experimental investigation, Phys. Fluids, 27, 369-380, https://doi.org/10.1017/jfm.2014.174, 2015.

Jensen, N.: A note on wind generator interaction, no. 2411 in Risø-M, Risø National Laboratory, ISBN 87-550-0971-9, 1983.

Kang, S., Yang, X., and Sotiropoulos, F.: On the onset of wake meandering for an axial flow turbine in a turbulent open channel flow, J. Fluid Mech., 744, 376–403, https://doi.org/10.1017/jfm.2014.82, 2014.

Katic, I., Hojstrup, J., and Jensen, N. O.: A simple model for cluster efficiency, in: Proceedings from the European Wind Energy Conference, pp. 407–410, Rome, Italy, 1986.

Kraushaar, M.: Application of the compressible and low-Mach number approaches to Large-Eddy Simulation of turbulent flows in aero-engines, Ph.D. thesis, INPT, https://theses.hal.science/file/index/docid/711480/filename/Kraushaar_.pdf, 2011.

Larsen, G. C.: A simple stationary semi-analytical wake model, Risø National Laboratory for Sustainable Energy, 2009.

Larsen, G. C., Madsen Aagaard, H., Bingöl, F., Mann, J., Ott, S., Sørensen, J. N., Okulov, V., Troldborg, N., Nielsen, N. M., Thomsen, K., Larsen, T. J., and Mikkelsen, R.: Dynamic wake meandering modeling, Risø National Laboratory, https://doi.org/10.1016/j.renene.2014.01.002, 2007.

https://doi.org/10.5194/wes-2025-264
Preprint. Discussion started: 4 December 2025

Li, Z., Dong, G., and Yang, X.: Onset of wake meandering for a floating offshore wind turbine under side-to-side motion, J. Fluid Mech., 934, https://doi.org/10.1017/jfm.2021.1147, 2022.

Lignarolo, L., Ragni, D., Scarano, F., Ferreira, C., and Bussel, G.: Tip-vortex instability and turbulent mixing in wind-turbine wakes, J. Fluid Mech., 781, 467–493, https://doi.org/10.1017/jfm.2014.82, 2015.

Mao, X. and Sørensen, J. N.: Far-wake meandering induced by atmospheric eddies in flow past a wind turbine, J. Fluid Mech., 846, 190–209, https://doi.org/10.1017/jfm.2018.275, 2018.

Martínez-Tossas, L., Churchfield, M., and Leonardi, S.: Large eddy simulations of the flow past wind turbines: actuator line and disk modeling, Wind Energy, 18, 1047–1060, https://doi.org/10.1002/we.1747, 2015.

Martínez-Tossas, L., Churchfield, M., and Meneveau, C.: Optimal Smoothing Length Scale for Actuator Line Models of Wind Turbine Blades Based on Gaussian Body Force Distribution, Wind Energy, 20, 1083–1096, https://doi.org/10.1002/we.2081, 2017.

Martínez-Tossas, L. A. and Meneveau, C.: Filtered lifting line theory and application to the actuator line model, J. Fluid Mech., 863, 269–292, https://doi.org/10.1017/jfm.2018.994, 2019.

Medici, D.: Experimental studies of wind turbine wakes: power optimisation and meandering, Ph.D. thesis, KTH, https://www.mech.kth.se/thesis/2006/phd/phd_2006_davide_medici.pdf, 2005.

Medici, D. and Alfredsson, P. H.: Measurements on a Wind Turbine Wake: 3D Effects and Bluff Body Vortex Shedding, Wind Energ., 9, 219–236, https://doi.org/10.1002/we.156, 2006.

Messmer, T., Hölling, M., and Peinke, J.: Enhanced recovery caused by nonlinear dynamics in the wake of a floating offshore wind turbine, J. Fluid Mech., 984, https://doi.org/10.1017/jfm.2024.175, 2024.

Meyer Forsting, A. R., Pirrung, G. R., and Ramos-García, N.: A vortex-based tip/smearing correction for the actuator line, Wind Energ. Sci., 4, 369–383, https://doi.org/10.5194/wes-4-369-2019, 2019.

Mikkelsen, R.: Actuator Disc Methods Applied to Wind Turbines, Ph.D. thesis, Technical University of Denmark, https://backend.orbit.dtu.dk/ws/portalfiles/portal/5452244/Robert.PDF, 2003.

Moureau, V., Domingo, P., and Vervisch, L.: Design of a massively parallel CFD code for complex geometries, Comptes Rendus Mécanique, 339, 1239–1250, https://doi.org/10.1016/j.crme.2010.12.001, 2011.

Okulov, V. L., Naumov, I. V., Mikkelsen, R. F., Kabardin, I. K., and N, S. J.: A regular Strouhal number for large-scale instability in the far wake of a rotor, J. Fluid Mech., 747, 369-380, https://doi.org/10.1017/jfm.2014.174, 2014.

Sorensen, J. N. and Shen, W. Z.: Numerical modeling of wind turbine wakes, J. Fluids Eng., 124, 393–399, 2002.

Troldborg, N., Sørensen, J., and Mikkelsen, R.: Actuator Line Modeling of Wind Turbine Wakes, Ph.D. thesis, Technical University of Denmark, https://backend.orbit.dtu.dk/ws/files/5289074/Thesis.pdf, 2009.

WindEurope: Europe can expect to have 10 GW of floating wind by 2030, https://windeurope.org/newsroom/news/europe-can-expect-to-have-10-gw-of-floating-wind-by-2030/, 2022.